Defining the Design Principles of Skin Epidermis Postnatal Growth

Dekoninck, Sophie

2020-04-30

Dekoninck , S , Hannezo , E , Sifrim , A , Miroshnikova , Y A , Aragona , M , Malfait , M , Gargouri , S , de Neunheuser , C , Dubois , C , Voet , T , Wickström , S A , Simons , B D & Blanpain , C 2020 , ' Defining the Design Principles of Skin Epidermis Postnatal Growth ' , Cell , vol. 181 , no. 3 , pp. 604-+ . https://doi.org/10.1016/j.cell.2020.03.015

http://hdl.handle.net/10138/315806
https://doi.org/10.1016/j.cell.2020.03.015

Article

Cell

Defining the Design Principles of Skin Epidermis Postnatal Growth

Graphical Abstract

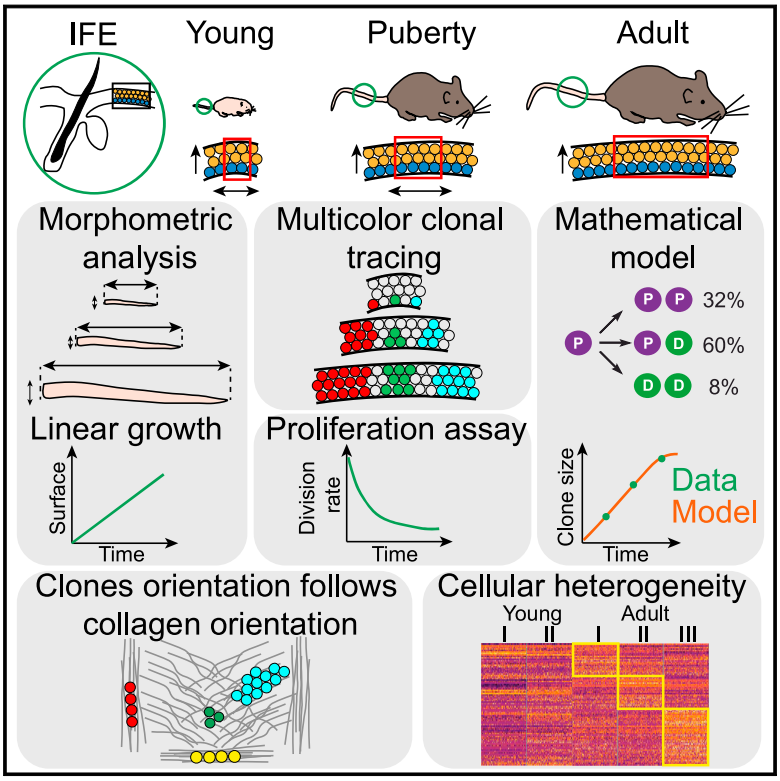

Authors

Sophie Dekoninck, Edouard Hannezo, Alejandro Sifrim, ..., Sara A. Wickström, Benjamin D. Simons, Cédric Blanpain

Correspondence

cedric.blanpain@ulb.ac.be

In Brief

During postnatal growth, tissues steadily grow until they achieve their final size. Looking at the interfollicular epidermis in mice, Dekoninck et al. find that progenitors present an excess of self-renewing division throughout the development. This imbalance, coupled with an ever-decreasing proliferation rate in both scale and interscale compartments, provides linear tissue expansion and maintenance of skin barrier function at the same time.

Highlights

- Linear growth of the epidermis during postnatal development
- Constant imbalance of self-renewal and decreasing proliferation leads to IFE growth
- Higher molecular homogeneity in developmental progenitors
- Orientation of clonal growth follows orientation of collagen fibers

Dekoninck et al., 2020, Cell *181*, 1–17
April 30, 2020
https://doi.org/10.1016/j.cell.2020.03.015

CellPress

Please cite this article in press as: Dekoninck et al., Defining the Design Principles of Skin Epidermis Postnatal Growth, Cell (2020), https://doi.org/10.1016/j.cell.2020.03.015

Article

Cell

Defining the Design Principles of Skin Epidermis Postnatal Growth

Sophie Dekoninck,[1,12] Edouard Hannezo,[2,3,12] Alejandro Sifrim,[4,5] Yekaterina A. Miroshnikova,[6,7,8] Mariaceleste Aragona,[1] Milan Malfait,[1] Souhir Gargouri,[1] Charlotte de Neunheuser,[1] Christine Dubois,[1] Thierry Voet,[4,5] Sara A. Wickström,[6,7,8] Benjamin D. Simons,[3,9,10] and Cédric Blanpain[1,11,13,*]

[1]Université Libre de Bruxelles, Laboratory of Stem Cells and Cancer, Brussels 1070, Belgium
[2]Institute of Science and Technology Austria, Am Campus 1, 3400 Klosterneuburg, Austria
[3]The Wellcome Trust/Cancer Research UK Gurdon Institute, University of Cambridge, Tennis Court Road, Cambridge CB2 1QN, UK
[4]Department of Human Genetics, University of Leuven, KU Leuven, Leuven, Belgium
[5]Wellcome Sanger Institute, Sanger Institute – EBI Single-Cell Genomics Centre, Hinxton, UK
[6]Helsinki Institute of Life Science, University of Helsinki, Biomedicum, Haartmaninkatu 8, 00290 Helsinki, Finland
[7]Wihuri Research Institute, Biomedicum, Haartmaninkatu 8, 00290 Helsinki, Finland
[8]Max Planck Institute for Biology of Ageing, Joseph Stelzmann Str. 9b, 50931 Cologne, Germany
[9]Cavendish Laboratory, Department of Physics, J. J. Thomson Avenue, Cambridge CB3 0HE, UK
[10]Wellcome Trust-Medical Research Council Stem Cell Institute, University of Cambridge, UK
[11]WELBIO, Université Libre de Bruxelles, Brussels 1070, Belgium
[12]These authors contributed equally
[13]Lead Contact
*Correspondence: cedric.blanpain@ulb.ac.be
https://doi.org/10.1016/j.cell.2020.03.015

SUMMARY

During embryonic and postnatal development, organs and tissues grow steadily to achieve their final size at the end of puberty. However, little is known about the cellular dynamics that mediate postnatal growth. By combining *in vivo* clonal lineage tracing, proliferation kinetics, single-cell transcriptomics, and *in vitro* micro-pattern experiments, we resolved the cellular dynamics taking place during postnatal skin epidermis expansion. Our data revealed that harmonious growth is engineered by a single population of developmental progenitors presenting a fixed fate imbalance of self-renewing divisions with an ever-decreasing proliferation rate. Single-cell RNA sequencing revealed that epidermal developmental progenitors form a more uniform population compared with adult stem and progenitor cells. Finally, we found that the spatial pattern of cell division orientation is dictated locally by the underlying collagen fiber orientation. Our results uncover a simple design principle of organ growth where progenitors and differentiated cells expand in harmony with their surrounding tissues.

INTRODUCTION

Organism growth is a key process that needs to be orchestrated harmoniously throughout development. Animal development starts from a single cell to form a multicellular organism composed of tissues containing different cell types. After the different cell types have been specified during embryonic development, the organs and tissues have to grow during postnatal life to achieve their final size at the end of puberty. In adult animals, cells lost by differentiation and cell death must be compensated by cell division in a process called tissue homeostasis. Over the last decade, great efforts have been made to understand the mechanisms controlling tissue homeostasis in adulthood. Lineage-tracing and clonal analyses have been instrumental in defining the clonal dynamics ensuring asymmetric renewal at the population level, maintaining the balance between proliferation and differentiation (Blanpain and Simons, 2013). In contrast, very little is known about the mechanisms that ensure postnatal growth from birth until animals reach their final size at the end of puberty. During postnatal growth, an imbalance between proliferation and differentiation is required to generate the excess of cells that fuels tissue expansion. How this imbalance is controlled and achieved is largely unknown.

The skin is the first barrier that protects animals against their microenvironment. The epidermis is composed of hair follicles (HFs) and their surrounding interfollicular epidermis (IFE). The IFE contains a single proliferative layer of basal cells (BCs) expressing keratin 14 and 5 (K14 and K5, respectively) and several suprabasal layers of terminally differentiated cells expressing K1 and K10 that progressively become enucleated and are shed as squames at the skin surface (Blanpain and Fuchs, 2006). To compensate for the loss of terminally differentiated cells, the IFE is constantly renewed by the proliferation of stem cells (SCs) and progenitors (Blanpain and Simons, 2013). The tail epidermis is a well-described tissue composed of two distinct regions (the scale and interscale) in which the clonal dynamics mediating adult tissue homeostasis have been studied extensively. Mouse tail IFE homeostasis is ensured by SCs and committed progenitors (CPs), which together balance self-renewal and differentiation in a stochastic manner at the

population level (Clayton et al., 2007; Mascré et al., 2012; Sánchez-Danés et al., 2016). In contrast, during postnatal growth and the concomitant expansion of the skin, SCs and/or progenitors need to adjust the balance between renewal and differentiation to expand the numbers of basal and suprabasal cells. The mechanisms responsible for controlling the imbalance of self-renewal over differentiation, which mediates skin expansion, are currently unknown.

Here we used the murine tail and paw epidermis to unravel the mechanisms that mediate postnatal skin expansion. Using a multidisciplinary approach, we define the pattern of cell fate decisions during tissue growth. We show that postnatal tail and paw skin expansion is mediated by a single population of equipotent developmental progenitors (DPs) that present a fixed fate imbalance of renewing divisions coupled with an ever-decreasing proliferation rate. We show that this strategy is optimal to ensure expansion of the basal progenitor cell pool while maintaining constant suprabasal thickness. We validate the model via clonal analysis performed at different time points during postnatal development. Finally, we demonstrate that the direction of clonal growth does not follow large-scale cues from anisotropic tail growth but local cues from the underlying collagen fiber orientation.

RESULTS

The IFE Expands Linearly during Postnatal Development

The mouse tail epidermis is composed of two regions that follow distinct differentiation programs: the interscale surrounds triplets of HFs and is characterized by suprabasal cells expressing K1 and K10, and the scale is characterized by expression of K31, K36, and K84 in differentiated cells (Didierjean et al., 1983; Tobiasch et al., 1992). In adult mice, these two regions behave as independent compartments that are sustained by their own pool of stem and progenitor cells (Gomez et al., 2013; Sánchez-Danés et al., 2016). However, how and when these SCs, progenitors, and their compartmentalization are specified during development remains unclear.

To address these questions, we first assessed macroscopic tail expansion by measuring the length, width, and total area of the tail from post-natal day 1 (P1) to P60. The results showed that the tail surface grew linearly from P1 to P30 by about 12-fold and then slowly reached a plateau. Most of the expansion was due to tail elongation (7-fold from P1 to P60), whereas its diameter increased only by 2.5-fold during the same period (Figures 1A–1E). Altogether, our data show that the tail surface increases 17-fold in a highly anisotropic fashion during neonatal growth.

We then defined postnatal tail expansion at the microscopic level. Using HF triplets as a reference frame, we measured the area of IFE covered by the scale and half of the two adjacent interscale regions, which we defined as the HF area (Figures 1A, 1B, and S1A–S1D). Because *de novo* HF formation does not occur after birth, the length and width of HF areas can be used as a proxy to measure local tissue expansion. We found that the distance between two HF lines along the antero-posterior (AP) axis increased more (7-fold from P1 to P60) than the distance between two adjacent HF follicle triplets along the left-right (LR) axis (2.3-fold from P1 to P60) (Figures 1F–1H). Altogether, the HF area expands around 16-fold from P1 to P60. Thus, macroscopic and microscopic measurements give statistically similar results, showing that the IFE surface expands uniformly from P1 to P60, with a linear increase from P1 to P30 (Figure 1I).

Lineage Tracing of DPs Recapitulates Tissue Growth

To define the spatio-temporal dynamics of IFE expansion at single-cell resolution, we performed clonal analysis using a multicolor lineage-tracing approach (Figures 2A and 2B). Tamoxifen (TAM) was administrated to *K14-CreER/Rosa-Confetti* mice at P1 at a dose that leads to fluorescent reporter expression in BCs sufficiently isolated from each other to be able to follow the fate and expansion of targeted individual cells. The numbers of BCs and suprabasal cells per clone were quantified at different time points in the scale and interscale (Figures 2C and 2D). In both compartments, clones grew rapidly from P1 to P30 and then more slowly from P30 to P60 (Figures 2E and 2F), mirroring the tail surface, with clone survival (or persistence) being globally stable from P7 to P60 in both scale and interscale (Figure 2G), a hallmark of unbalanced clonal expansion via self-renewing divisions of BCs. Importantly, the overall increase in clone size well matched the overall tissue expansion (Figure 2H), and the BC size did not change over time (Figure S1D), demonstrating that the cells we targeted in our lineage-tracing experiments are representative of those that drive whole-tissue expansion.

Interestingly, we found that scale clones were consistently larger than interscale clones at all time points (21-fold versus 10-fold expansion from P1 to P30; P7, $p = 0.007$; P15, $p < 0.0001$; P30, $p < 0.0001$; Mann-Whitney test), which could not be attributed to differential clone loss (Figure 2G). Moreover, the cumulative basal clone size distributions of interscale and scale clones fitted well with a single exponential dependence at all time points (Figures 2I and 2J). This observation arises as a hallmark of stochastic cell fate choices from single populations of DPs, which mediate post-natal growth reliant (Klein and Simons, 2011).

Ever-Decreasing Proliferation Rate of DPs during Postnatal Growth

To ensure the quasi-linear growth of tissue supported by a single population of DPs, these cells must either progressively decrease the proportion of self-renewing division over commitment to terminal differentiation or smoothly adjust their proliferation rate and transit time from the basal layer to the cornified layer (or potentially both). To discriminate between these possibilities, we performed quantitative label dilution experiments using *K5tetOFF/Tet-O-H2BGFP* mice (Mascré et al., 2012; Sada et al., 2016; Tumbar et al., 2004; Zhang et al., 2009) at different time points during postnatal development. In the absence of doxycycline (Dox), H2B-GFP was homogenously expressed at a high level in all BCs (Figures S2A–S2C). H2B-GFP expression was chased by administration of Dox starting at P1, P7, P21, or P30, and the level of H2B-GFP label dilution in BCs, representing the number of cell divisions accomplished during the chase period, was quantified by fluorescence-activated cell sorting (FACS) at different time points (Figures S2D–S2G). These data showed that the rate of cell division decreased during postnatal

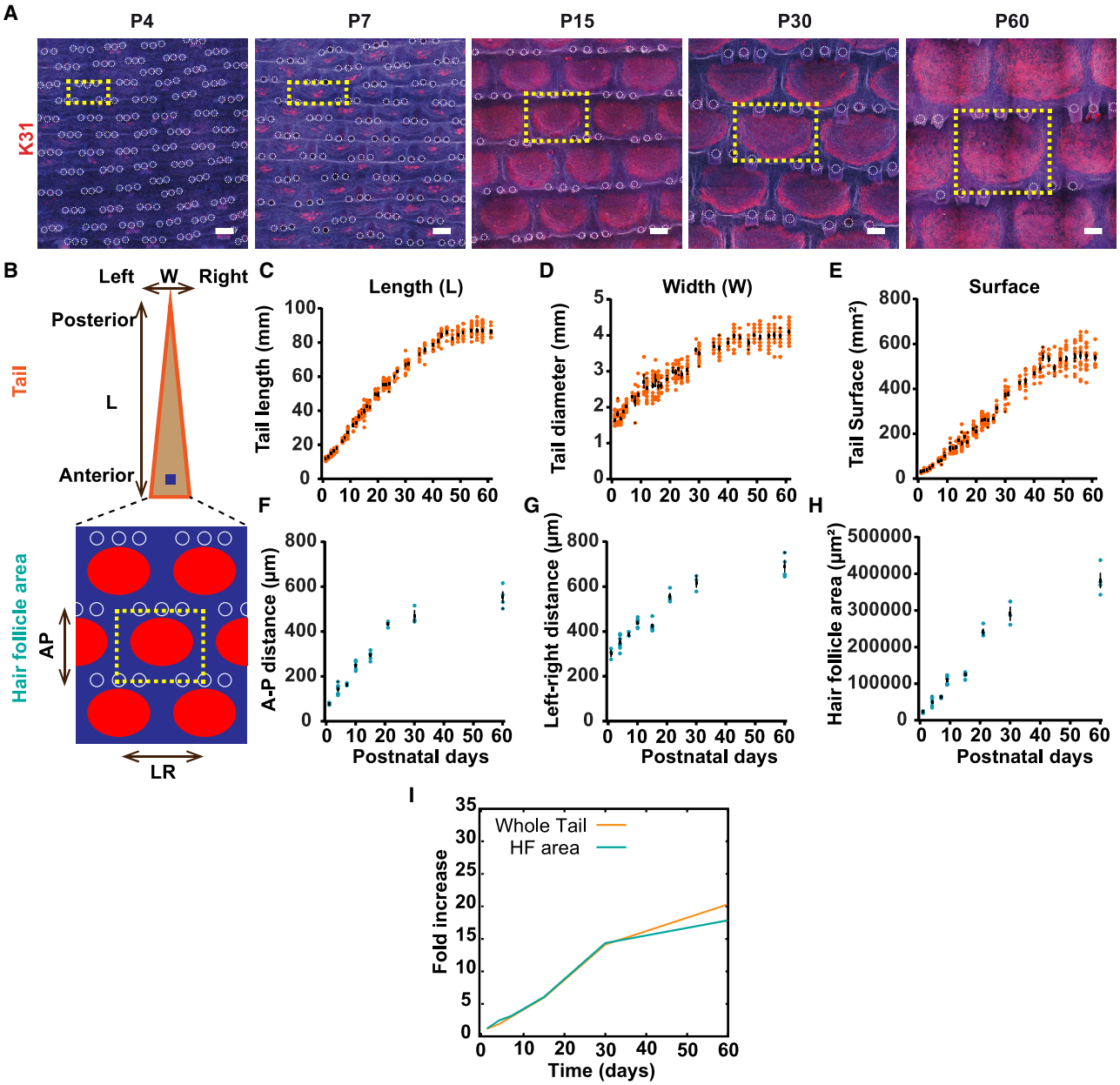

Figure 1. The IFE Expands Linearly during Postnatal Development

(A) Representative immunostaining of K31 in whole-mount tail epidermis, showing the scale (K31+) and interscale (K31−) regions at the given time points (maximum-intensity projection of confocal images). Yellow dotted lines, HF area; white circles, HFs. Nuclei are stained with Hoechst. Scale bars, 100 µm.

(B) Diagram of the tail epidermis showing its AP axis. Below is a scheme representing the scale (red) and interscale (blue) regions. Yellow rectangle, HF area; L, length; W, width; white circles, HFs.

(C–E) Measurement of L (C), W (D), and calculated total surface of the tail (E) from P1 to P60 ($n \geq 5$ mice per time point).

(F–H) Measurement of the AP (F) and LR (G) distances and the calculated surface of the HF area (H) from P1 to P60 ($n \geq 3$ mice per time point).

(I) Calculated fold increase of the tail surface (orange) and the HF area (cyan) from P1 to P60.

Data are represented as mean ± SEM. See also Figure S1.

development, with an average cell cycle time estimated to be around 1.2 days between P1 and P7, 1.9 days between P7 and P15, 4.1 days between P21 and P28 (Figures S2H and S2I), and 6.5 days at P60 (Mascré et al., 2012). Of note, we did not observe a significant slowly cycling population of BCs during post-natal tissue expansion (Figures S2D and S2E), in support of the idea of a single population of DPs.

Although the H2B-GFP label dilution data show that the rate of DP cell division decreases over time, FACS quantification cannot discriminate whether differential expansion of clones in the scale

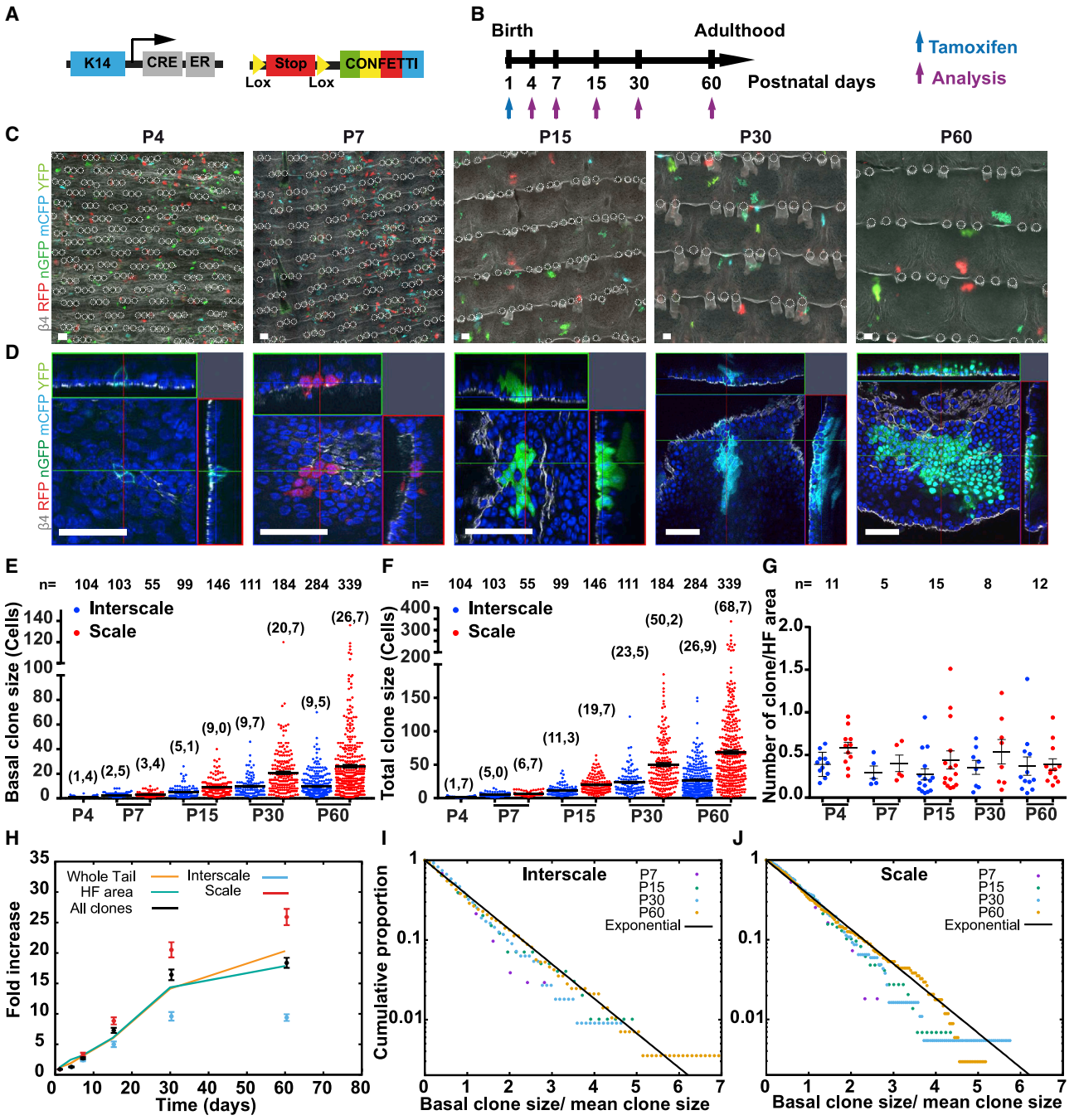

Figure 2. Lineage Tracing of DPs Recapitulates Tissue Growth

(A) Genetic strategy used to target multicolor Confetti expression in K14-expressing BCs.

(B) Protocol used to study the fate of BCs targeted at birth (P1).

(C) Representative *K14-CreER/Rosa-Confetti* whole-mount tail epidermis collected at the given time points, induced clonally at P1 (maximum-intensity projection of confocal images). Scale bars, 50 μm.

(D) Confocal images showing Confetti clones from P4 to P60. Scale bars, 50 μm.

(E and F) Quantification of the number of basal (E) and total (F) cells per clone in interscale and scale. n, number of analyzed clones; brackets, average clone size.

(G) Quantification of the number of clones per HF area in interscale and scale. n, number of mice.

(H) Graph showing the basal clone size from scale and interscale and all clones normalized to their relative surface area, the expansion of the whole tail surface, and HF area. Scale clones are larger than interscale clones (P7, $p = 0.007$; P15, $p < 0.0001$; P30, $p < 0.0001$; Mann-Whitney test).

(legend continued on next page)

and interscale regions is mediated by a difference in the rate of cell proliferation or a different imbalance toward symmetrical division. To discriminate between these two possibilities, we turned to cell proliferation kinetics measurements using 5-ethynyl-2′-deoxyuridine (EdU)/bromodeoxyuridine (BrdU) double-labeling experiments allowing us to define whether cell cycle time is regulated in a region-specific manner during postnatal development. EdU was administrated first at P4, P7, P15, P30, and P60, and then BrdU was given continuously to measure the proportion of double-labeled cells (and the proportion of suprabasal EdU+ cells) at different time points in the scale and interscale (Figures 3A–3O and S2J), which fitted well with a single population of dividing cell with a refractory period in each region. These results confirmed that the rate of cell cycle re-entry decreases over time and demonstrated that DPs consistently cycle faster in the scale than in the interscale (Figures 3N–3P), similar to their differential proliferation rate during adult homeostasis (Gomez et al., 2013; Mascré et al., 2012; Sada et al., 2016; Sánchez-Danés et al., 2016; Spearman and Garretts, 1966). Indeed, we reasoned that the progressive and constant decrease in DP proliferation rate during postnatal growth could explain the linear rather than exponential growth of the tail epidermis and the differential scale-interscale growth.

To determine whether a cell-autonomous or non-autonomous mechanism controls the ever-decreasing rate of proliferation observed during postnatal development, we assessed the proliferation rate of primary keratinocytes freshly isolated from mice of different ages and cultured *in vitro* for 48 h on fibronectin- and collagen-coated plates. Quantification of BrdU incorporation by FACS analysis showed that proliferation of cultured keratinocytes decreased with the age of the mice, similar to what we found *in vivo* (Figures 3Q, S2K, and S2L). These data suggest that the decrease in proliferation of keratinocytes is not a consequence of a higher level of growth hormones in the serum of young mice but a consequence of keratinocyte-autonomous mechanisms. These results do not rule out the possibility that growth hormones modify the epigenetic and transcriptional landscape of the keratinocytes, rendering them more responsive to growth factors.

A Constant Excess of Symmetric Renewing Division Mediates Postnatal Development

The increase in the number of BCs per clone combined with stable clonal persistence can only be achieved if DPs increase their number of symmetric renewing divisions at the expense of symmetric differentiation, creating an imbalance in favor of self-renewal. To test whether adjustment of the proliferation rate over time is sufficient to quantitatively explain the spatio-temporal dynamics of postnatal growth, we turned to quantitative modeling of the lineage tracing data (STAR Methods). Taking the experimentally measured proliferation rate as input to the model and considering the observation that rescaled clone size distributions are consistently well-fitted by a single exponential, we explored whether the average clone size and clonal persistence could be explained by a minimal model consisting of a single equipotent DP population characterized by stochastic fate behavior.

In an out-of-homeostasis setting, clonal dynamics are only weakly dependent on the probability of asymmetric division (1-2r) and pre-dominantly dependent on the product of $\Delta\lambda$, where Δ is the degree of imbalance between symmetric divisions (here, self-renewing and differentiation divisions), and λ is the cell division rate (STAR Methods). One should note that the results of these models are also largely insensitive to the nature of fate regulation (for instance, intrinsic versus extrinsic fate choices or whether differentiation feeds back on or is mediated by cellular proliferation events). Interestingly, based on the measured cell division rate, we found that a constant fate imbalance of $\Delta = 24\% \pm 4\%$ (best fit ± 95% confidence interval) provided a very good fit for the quasi-linear P1 to P30 growth dynamics of interscale clones (Figures 4A and 4B). Moreover, the model also provided a good prediction for clonal persistence, showing an initial decrease followed by a plateau (Figure 4C), characteristic of imbalanced cell fates (STAR Methods). Even more surprisingly, modeling of scale clones showed that the same constant fate imbalance, $\Delta = 24\% \pm 2\%$ (best fit ± 95% confidence interval) provided a very good fit for the clone size across the course of postnatal growth (Figures 4D–4F). This means that the 2-fold enhancement of clonal growth in scale could be explained by the observed faster proliferation rate compared with interscale. These data suggest that scale and interscale compartments are each sustained by a single population of DPs that undergo an excess of symmetric renewing divisions and acquire different proliferation rates during post-natal development, depending on their localization.

To experimentally challenge this simple constant fate imbalance model, we performed an additional lineage-tracing experiment at P15, chasing clones for 4 and 14 days (Figures 4G–4U). In interscale, clones increased their average basal size by a factor of 1.9 and their average total size by a factor of 4.1 in 2 weeks (Figures 4J, 4L, 4N, and 4O). Interestingly, this average clone size expansion, together with the persistence evolution from P4 to P15, fitted well with the model prediction (Figures 4R–4T). Similarly, scale clones increased their basal content by a factor of 2.9 and their total content by a factor of 6.2, which also fitted well with the model prediction in terms of average clone size and persistence (Figures 4K, 4M, 4P, 4Q, 4S, and 4U). These data confirm that epidermal cells do not change their cell fate imbalance during the growth process.

We then assessed whether this mechanism of tissue growth (fixed imbalance of self-renewal combined with a progressively decreasing proliferation rate) uncovered in the tail epidermis is a general strategy of stratified epithelial postnatal expansion. To this end, we studied, at single-cell resolution, the cellular mechanisms that mediate postnatal growth in the paw epidermis. We performed clonal analysis using *K14-CreER/Rosa-Confetti*

(I and J) Cumulative distributions of interscale (I) and scale (J) basal clone size, rescaled by average clone size at all time points and well described by a simple exponential distribution (black line).
Data are represented as mean ± SEM.

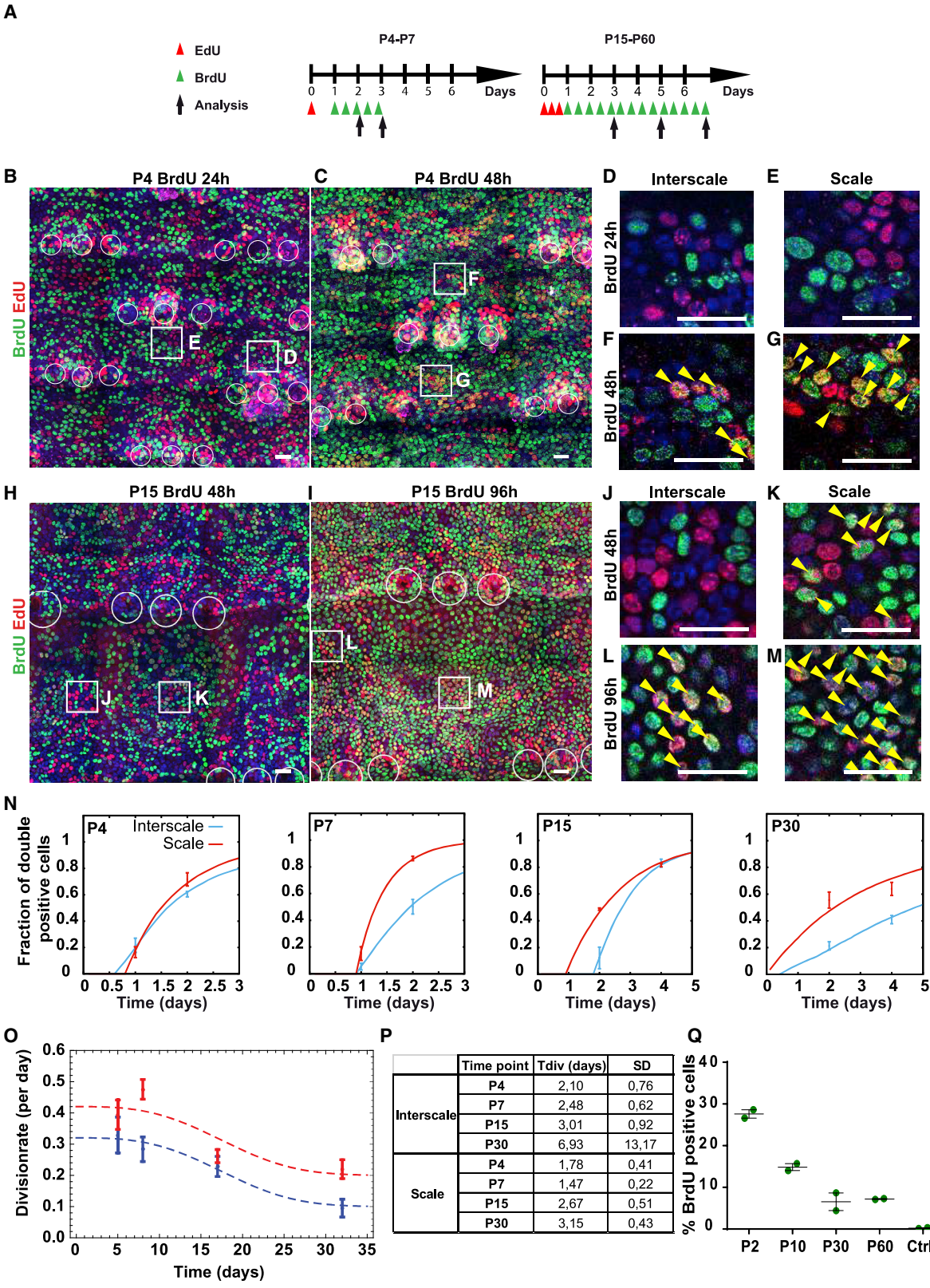

	Time point	Tdiv (days)	SD
Interscale	P4	2,10	0,76
	P7	2,48	0,62
	P15	3,01	0,92
	P30	6,93	13,17
Scale	P4	1,78	0,41
	P7	1,47	0,22
	P15	2,67	0,51
	P30	3,15	0,43

(legend on next page)

mice induced at P1 and assessed the clonal behavior of individual BCs at P4, P7, P15, P30, and P60 in relation to the length and width of the paw area. The paw area expanded by a factor of 6.1 from P1 to P60 and in a more isotropic manner compared with the tail (2.7× in length, 2.4× in width) (Figures S3A–S3D). Most of the paw expansion occurred in a nearly linear manner, although it reached its plateau earlier than in the tail (Figure 1I). We performed a single BrdU pulse and quantified the proportion of labeled cells after 4 h, which can be used to approximate the proliferation rate (Figure S3E; STAR Methods). Interestingly, the proportion of BrdU-labeled cells decreased from P1 to P15, going from 29.8% ± 2.3% of labeled cells at P1 to 12.0% ± 1.9% at P15 and then remained stable from P15 to P60 (Figure S3F). Clonal analysis of the paw epidermis showed that the basal content of the clones expanded 5.8× from P1 to P15 (Figures S3G–S3K), mirroring the paw tissue expansion, and that clone size distributions were well fitted at all time points by a single exponential, a hallmark of a single population of DPs being responsible for the skin expansion (Figure S3L). Implementing a similar theoretical model as before (with the proliferation rates measured in the paw) showed that the clone size and persistence time course data were well fitted by the same constant imbalance model proposed for the tail, with an imbalance of 20% from P1 to P15 (STAR Methods; Figures S3M–S3O), demonstrating that the design principles uncovered in the tail epidermis also account for skin expansion in the paw epidermis.

A Constant Imbalance Mediates Harmonious Tissue Expansion

Our data and modeling approaches suggest that DPs adjust only their division rate to match the spatio-temporally varying patterns of tissue growth while keeping their imbalance in fate choices approximately constant. Why would such a strategy be implemented and selected in several epidermal compartments? One possibility is that such a state of constant imbalance toward symmetric renewal represents a stable, cell-intrinsic ground state for DPs (Mojtahedi et al., 2016). However, we postulated that the observed growth strategy could also be explained mechanistically by considering a simple optimality criterion for epidermal growth.

We reasoned that, if the only constraint in the system is expansion of the basal layer at a prescribed speed, then this can be achieved in many ways (Figures 5A–5D; STAR Methods). For instance, DPs could retain balanced cell fate choices throughout development, similar to homeostasis but with a higher division rate, producing only differentiated cells that would accumulate both in the basal and suprabasal layer and, thus, lead to dilution of the basal DP pool, as observed in *Drosophila* intestinal regeneration (Jin et al., 2017; Figure 5A). However, our H2B-GFP dilution experiments did not show such an accumulation of differentiated cells (Figure S2). A second possibility would be that DPs first undergo a phase of purely symmetric divisions to rapidly expand the DP pool and then switch to a second phase of asymmetrical divisions to generate differentiated cells. This so-called "bang-bang" mechanism has been proposed to be optimal for rapid formation of mouse intestinal crypts after birth (Itzkovitz et al., 2012; Figure 5B). However, our clonal data initiated at P1 show that differentiated cells are produced early after birth (Figures 2E and 2F). Finally, although our proliferation experiments rule out this hypothesis, a constant division rate similar to homeostasis (one division every 4–5 days) would be sufficient to give rise to the observed linear growth if the imbalance was close to 100% around birth and subsequently continuously decreases (Figure 5C). Interestingly, all of these scenarios lead either to dilution of the DP (Figure 5A) or to a phase in which very few suprabasal cells are produced, leading to skin thinning during expansion and potentially compromising skin barrier function (Figures 5B and 5C; see more explanations in STAR Methods). We thus explored the consequences of a very simple design principle of epidermal growth: that the basal area must grow (in response to the growth of the underlying tissue) by a prescribed amount but also that the ratio of suprabasal cells to BCs must remain constant (to ensure sufficient epidermal thickness throughout the expansion phase). Strikingly, imposing these two constraints was only compatible with a single theoretical growth scenario characterized by (1) near-constant fate imbalance and (2) continually decreasing division rates to adjust to growth characteristics (Figure 5D; STAR Methods). This design principle thus provides a simple and robust explanation for the experimentally observed clonal dynamics, which we explored quantitatively.

Before going further toward a quantitative comparison of this optimality criterion with the data, we sought to verify whether its assumptions apply. For this, we measured the ratio of suprabasal cells to BCs at all time points in tail scale and interscale as well as in the paw. Importantly, we found that this ratio was

Figure 3. Ever-Decreasing Proliferation Rate of DPs during Postnatal Growth

(A) Protocol of the EdU/BrdU double-labeling experiments.

(B–G) Representative P4 whole-mount tail epidermis at the given time points (B and C) (maximum-intensity projection of confocal images) and higher magnification of BCs in interscale (D and F) and scale (E and G) at the same time points.

(H–M) Representative P15 whole-mount tail epidermis at the given time points (H and I) (maximum-intensity projection of confocal images) and higher magnification of BCs in interscale (J and L) and scale (K and M) at the same time points. Yellow arrowheads, EdU/BrdU double-labeled cells; white circles, HFs. Nuclei are stained with Hoechst. Scale bars, 50 μm.

(N) Quantification of EdU/BrdU double-positive BCs in scale and interscale ($n \geq 3$ mice). Symbols, experimental data; lines, theoretical fits from a model of stochastic division after a refractory phase. Data are represented as mean ± SEM.

(O) Time evolution of the division rate in scale (red) and interscale (blue) BCs from P1 to P30. Symbols, experimental data; dashed lines, fit of the decrease in division rate over time, used for subsequent clonal modeling; error bars are mean ± SD.

(P) Average division time (TDiv) of epidermal BCs in interscale and scale, calculated from EdU/BrdU analysis.

(Q) Quantification of BrdU+ primary keratinocytes isolated from P2, P10, P30, and P60 mice, cultured for 48 h and incubated for 2 h with BrdU (n = 2 experiments). Error bars are mean ± SD.

See also Figure S2.

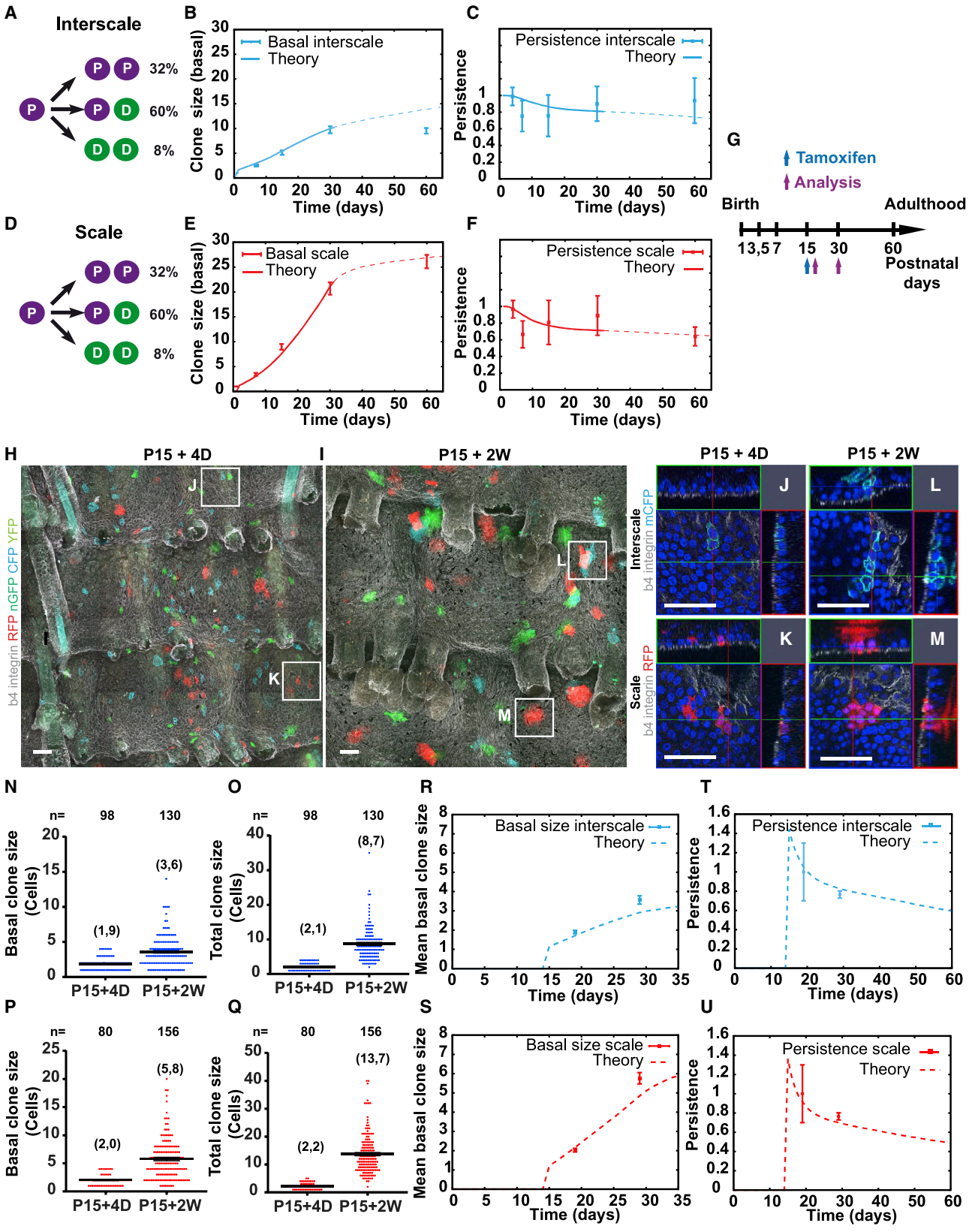

(legend on next page)

approximately constant across the growth phase (Figures 5E and 5F), validating the key assumption of the model. Moreover, in the tail, the ratio was equivalent in tail scale and interscale, although both regions displayed a 2-fold difference in the degree of growth (Figures 2E, 2F, and 2H). We then sought to test the hypothesis of constant imbalance by fitting the clonal data piece-wise to infer different values of imbalance (STAR Methods). Interestingly, we found that the inferred imbalance at each time point was close to its globally fitted value (Figures 5G and 5H). Finally, to see whether the other possible scenario could also fit our experimental data, we performed a sensitivity analysis to predict the time evolution of the BC density and suprabasal/basal ratio for each scenario (Figures S4A–S4D). Strikingly, this analysis confirmed that our constant imbalance model was the best-fitting scenario (STAR Methods).

With a single fitting parameter (suprabasal loss rate, which we set as constant across compartments but which has only weak effects on the resulting dynamics), our design principle could then quantitatively predict the following data: (1) the experimentally inferred imbalance at each time point (i.e., the fact that it should be constant in time and identical in scale and interscale despite their differential growth rate) and (2) the experimentally measured evolution of the division rate in scale and interscale as well as the observed enhanced division rate in scale throughout the growth phase (Figures 5G, 5H, and S4). This argues that the evolution of the proliferation kinetics and fate choices of DPs throughout growth can be predicted from simple principles and suggests that they are optimized for harmonious and coordinated basal and suprabasal expansion.

Transition between Postnatal Expansion and Adult Homeostasis

As mentioned above, the global growth kinetics of the tail slow down drastically after P30, a feature reflected in clone size evolution. Indeed, turning to a modeling approach for P30–P60 clone size evolution, first in scale regions, we found that this was consistent with the homeostatic model we proposed previously (Sánchez-Danés et al., 2016), characterized by perfectly balanced fate choices of a single CP population (Figure S5A, right). This argues for a transition from imbalanced to balanced cellular behavior occurring around or soon after P30. Turning to interscale regions, although P1 inductions do not provide the resolution to detect the appearance of the SC/CP hierarchy, P30–P60 clone size evolution was also consistent with a sharp transition toward a homeostatic, balanced cell fate around P30 because using the homeostatic SC/CP model provided a good fit for the data, albeit with an increased fate imbalance toward differentiation from CP compared with homeostasis (Figure S5A, left).

To further test these findings, we performed an additional lineage tracing experiment at P30, chasing clones for 4 days and 4 weeks (Figures S5B–S5P). Consistent with their lower proliferation rate, interscale clones only increased their average basal size by 2-fold and their average total size by 5.3-fold in 4 weeks (Figures S5E, S5G, S5I, and S5J). The homeostatic model accurately predicted the average clone size and clone persistence (Figures S5M and S5N). Likewise, scale clones increased 2.4× their basal content and 6.2× their total content in 4 weeks (Figures S5F, S5H, S5K, and S5L). Again, scale clone sizes and persistence were consistently well fitted by the model (Figures S5O and S5P). These data suggest a transition from imbalanced to balanced cell fate occurring around P30 in both scale and interscale and that the clonal dynamics of SCs in the interscale (Sánchez-Danés et al., 2016) arises late in development, presumably during the transition phase toward homeostasis.

Single-Cell RNA Sequencing of Post-natal and Adult Tail Epidermis

To define the molecular features associated with DPs and compare them with adult SCs and/or CPs (SC/CP) in homeostasis, we performed single-cell RNA sequencing of FACS-isolated basal tail keratinocytes depleted from HF cells (STAR Methods) of young (P7, n = 9.389 after quality control [QC]) and adult (P60, n = 10.447 after QC) mice using 10X Genomics technology (Zheng et al., 2017). We performed unsupervised clustering and excluded the cell clusters of the infundibulum (*Sox9*^{high}, *Krt17*^{high}, and *Krt79*^{high}), sebaceous gland cells (*Scd1*^{high}, *Mgst1*^{high}, and *Elovl6*^{high}), as well as cells containing a high content of mitochondrial genes, such as *mt-Co1* (dying cells) and performed further bioinformatics analysis on IFE cells (Joost et al., 2016). After processing, 6,102 and 7,551 cells for P7 and P60, respectively, were analyzed further (STAR Methods). We performed unsupervised clustering on individual samples using Seurat (Butler et al., 2018) and assessed the better level of resolution based on biological criteria (Figures 6A and 6B, left panels; STAR Methods). To better compare the young and adult epidermis, we also combined the two datasets using Harmony (Korsunsky et al., 2019; Tran et al., 2020), a method of batch

Figure 4. A Constant Excess of Symmetric Renewing Division Mediates Postnatal Development

(A–F) Theoretical modeling of the *K14-CreER/Rosa-Confetti* clonal data. A single population of DPs undergoes stochastic fate choices with a constant imbalance of Δ = 24% in favor of self-renewing division (PP) compared to differentiation (DD), together with an ever-decreasing proliferation rate between P1 and P30, in interscale (A) and scale (D). This model fits well with the measured expansion of basal clone size (B and E) and clonal persistence (C and F) in each region. Symbols, experimental data; lines, model prediction (thick line, P1–P30 model; thin dashed line, P30–P60 homeostatic model).

(G) Experimental design used to challenge the theoretical model.

(H and I) Representative *K14-CreER/Rosa-Confetti* epidermis analyzed 4 days (H) and 2 weeks (I) after TAM injection at P15 (maximum-intensity projection of confocal images).

(J–M) Confocal images of representative clones in interscale (J and L) and scale (K and M) 4 days and 2 weeks after TAM injection. Scale bars, 50 μm.

(N–Q) Quantification of interscale (N and O) and scale (P and Q) basal (N and P) and total (O and Q) clone size over time (n = 5 mice). N, number of analyzed clones; brackets, average clone size.

(R–U) The theoretical model well predicts the experimental measures of basal clone size expansion (R and S) and clonal persistence (T and U) in interscale (R and T) and scale (S and U) 4 days and 2 weeks after TAM administration to P15 mice. Symbols, experimental data; dashed lines, model predictions.

Data are represented as mean ± SEM. See also Figures S3 and S5.

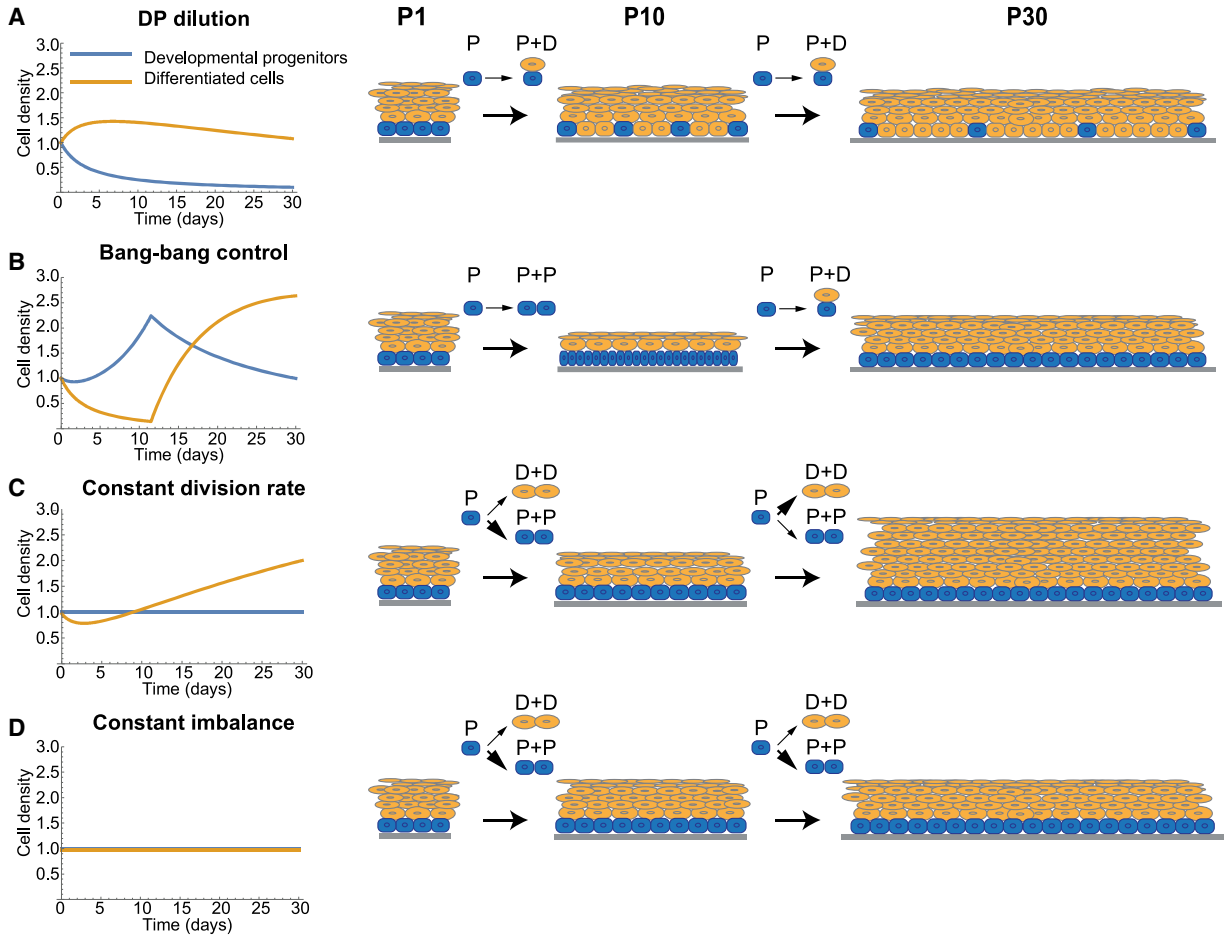

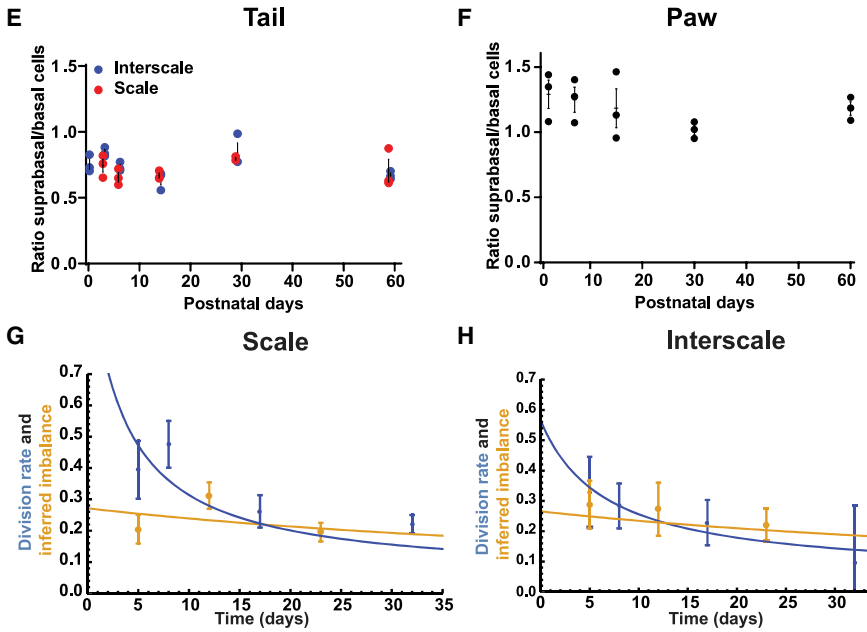

(legend on next page)

integration suited for datasets containing continuous transitioning between cell types or states, and annotated the clusters according to the individual clustering (Figures 6A and 6B, right panels). Interestingly, consistent with the modeling of the clonal fate data, individual clustering analysis revealed that young IFE cells were more homogeneous compared with adult IFE cells (Figures 6A and 6B). At P7, BCs, defined by their high expression for *Krt5* (Figure 6C), could be subclustered according to their different stages of the cell cycle (G1-S, cluster 3; S-G2-M, cluster 2; late G2-M, cluster 4; Figures 6A–6F and S6A; STAR Methods) and to their higher expression of known basal SC markers such as *Ccnd2*, *Col17a1*, and *Sparc*, which highlighted two populations in G0 (DP G0, one main cluster 0 and one smaller cluster 5; Figures 6G–6I; Joost et al., 2016; Liu et al., 2019). More committed cells were defined by their expression of differentiated markers such as *Sbsn* (committed and differentiated cells, cluster 1; Figure 6J). Similarly, adult tail epidermis clustering displayed BC cell-cycle-related clusters (G1-S, cluster 3; G2-M, cluster 4; Figures 6B–6F and S6B) as well as committed BCs expressing *Krt5* and *Krt1* (cluster 0; Figures 6B, 6C, and 6K). Two clusters of differentiated cells were found, corresponding to the interscale regions enriched for *Krt1* and *Krt10* expression (cluster 5) and scale region (cluster 7), expressing higher levels of the scale markers *Krt36* and *Krt84* (Figures 6B, 6K, 6L, and S6B), not expressed in the young sample, as predicted by the progressive appearance of scale markers during postnatal growth (Gomez et al., 2013; Tobiasch et al., 1992). In contrast, clustering of the adult tail epidermis uncovered that BCs in G0 could be subdivided into 3 distinct clusters (1, 2, and 6) associated with distinct signatures. G0 cluster 1, called SC/CP G0 (I), similar to what we found in P7, expressed higher level of *Sostdc1*, *Postn*, or *Ifitm3* (Figures 6M and S6B). The second G0 cluster (cluster 2, SC/CP G0 II) expressed higher levels of *Mt1/2*, *Tsc22d1*, or *Dcn* (Figures 6N and S6B), and the third cluster (cluster 6, SC/P G0 III) expressed higher levels of *Wnt*-related genes such as *Wnt3, Wnt4, Wnt10a, Wls* as well as *Igfbp2, 3, 7*, *Il1r2*, and *Tgm3* (Figures 6O and S6B). Interestingly, the genes of these two last specific clusters were expressed by the DP G0 II in P7 samples, suggesting a higher molecular segregation or heterogeneity of BCs in adults (Figures 6N, 6O, and S6A). Some small clusters (6, 7, and 8; Figures 6A and 6B) were still high for *Krt17* and *Sox9* or expressed high level of *Krt6* and were considered infundibulum cells in G2-M and companion layer cells (Figures S6A and S6B). SCENIC analysis (Aibar et al., 2017), which allows prediction of active transcription factors (TFs) and their putative target genes that control the identity of these stem and progenitor populations as well as their differentiated cells, showed that DPs are enriched for regulons associated with *Jun*, *Fos*, or *Trp63* (Figures S6C–S6E), whereas committed and differentiated cells are enriched for *Klf4* and *Klf5* and *Hes1* (Figures S6F and S6G), consistent with the well-established role of the Notch pathways and these TFs in promoting skin stratification (Blanpain and Fuchs, 2006). Finally, lineage trajectory analysis using Slingshot (Street et al., 2018) revealed one differentiation path at P7 and 2 differentiation paths (scale and interscale) in adults, allowed us to separate the different cell clusters according to their commitment, and showed one path from the SC/CP G0 (I) to the SC/CP G0 (III) subpopulations (Figure 6P). Altogether, these single-cell RNA sequencing data further support the existence of a more homogeneous population of DPs during postnatal skin expansion and the increase in cellular heterogeneity during transition to adult IFE homeostasis. To define when this cellular heterogeneity emerges, we performed single-cell RNA sequencing on the tail epidermis of a young adult mouse, at P30, when the clonal dynamics change from growth to homeostasis. After quality control filtering, we analyzed the expression of all markers identified in the adult SC/CP populations and compared them with the basal populations of P7 and P30 samples (Figure S6H). As expected, the differences between the two BC populations at P7 were minor, supporting a higher molecular homogeneity within the basal compartment compared with adults. Markers of adult SC/CP G0 I, such as *Sostdc1* and *Ifitm3*, were more highly expressed in a fraction of BCs in all three samples, defining the BC population I in all 3 datasets (Figure S6H). As mentioned previously, some markers from the adult SC/CP G0 II and III (such as *Dcn*, *Igfbp2*, and *Wnt4*) were co-expressed within the second population of DPs at P7 (DP G0 II), whereas most of the remaining markers were only weakly expressed. At P30, larger amounts of SC/CP G0 II markers (*Dcn*, *Mt1*, *Mt2*, *Gpha2*, and *S100a6*) were highly expressed in the P30 SC/CP G0 II population but still co-expressed with SC/CP G0 III markers (*Igfbp2*, *Igfbp7*, and *Wnt4*) (Figure S6H). Finally, the three SC/CP G0 populations were molecularly distinct at P60 (Figure S6H). To better visualize the difference in cellular heterogeneity of basal epidermal cells between the 3 time points, BCs were plotted according to their area under the curve (AUC) values for the markers specific for adult SC/CP G0 II (x axis) and III (y axis) (Figures S6I–S6K;

Figure 5. A Constant Imbalance Mediates Harmonious Tissue Expansion

(A–D) Schematics of possible design principles underlying epidermal expansion (imposed by growth of the tail) (STAR Methods). The epidermis could grow following balanced cell fates and a higher proliferation rate (A), which would lead to accumulation of non-dividing differentiated cells in the basal layer and DP dilution. In the case of the bang-bang control mechanism (B), DPs would achieve only symmetrical renewal during a first period and produce an overshoot of DPs without any new suprabasal cells produced. In a second period, DPs would achieve only asymmetrical divisions to re-establish the suprabasal layers. In a constant division rate scenario (C), DPs would keep a constant division rate but always change their cell fate outcome. In contrast with the other scenarios, a constant imbalance (D) accompanied by a decreasing proliferation rate would enable production of new DPs and sustain suprabasal cell density along the growth.

(E and F) Quantification of the number of suprabasal cells compared with the number of BCs in tail (E) and paw (F) epidermis (n = 3 mice per time point). Error bars are mean ± SEM.

(G and H) Time evolution of the measured division rate (blue dots, from Figure 3O) and piece-wise inferred imbalance (orange dots, from clonal data) compared with the theory prediction (thick lines) in scale (G) and interscale (H) after entering the overall growth rates of the two regions (from Figure 1) in the model. Theory of tissue expansion with the constraints of maintaining basal and suprabasal density constant predicts a nearly constant imbalance rate (orange line) and a constantly decaying division rate (blue line). Error bars are mean ± SD.

See also Figure S4 and STAR Methods.

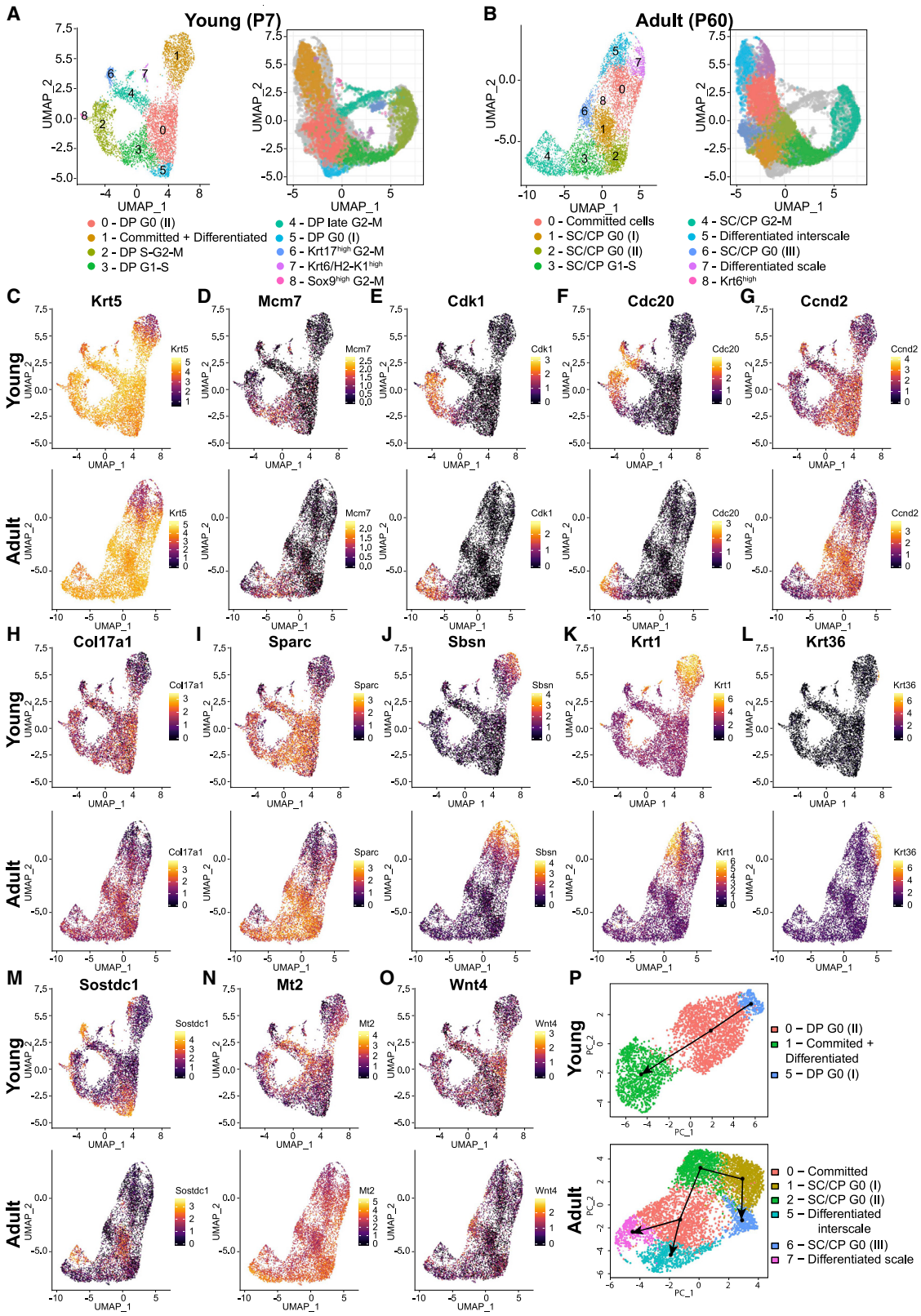

(legend on next page)

STAR Methods). Although all BCs showed a linear correlation between the two AUC values in the young sample, some BCs, in contrast, already started to deviate from the trend at P30 and even more strongly in the adult sample (Figures S6I–S6K). Altogether, these data show that BCs of the tail epidermis are more homogeneous during early postnatal development and that cellular heterogeneity begins around P30, at the time of the transition from a growing to a homeostatic mode of division, and further increased until mice reach their final size. These data provide important molecular insights into the genes that control stem and progenitor heterogeneity and their differentiation during postnatal development and adult homeostasis.

The Local Collagen Pattern in the Dermis Determines Clone Orientation and Cell Division

Our constant imbalance model helps us to understand the principles behind the regulation of cell fate decisions, in terms of fate outcomes and division rate, for a globally expanding tissue. However, it does not take into account the geometry of these choices, such as regulation of the cell division axis. Although our clonal analysis data showed that DPs undergo a high proportion of symmetric self-renewal, closer observation of our clones suggests that the spatial localization of two DPs after division is not random. In a simple anisotropic growing epithelium, one could expect clones to be oriented in the direction of net growth. However, clones within the tail epidermis revealed a more complex geometrical pattern. During postnatal expansion, a fraction of clones was isotropic and grew equally in every direction (Figure S7A), whereas other clones were anisotropic, growing preferentially in one direction, either parallel to the AP axis or to the LR axis of the tail. This prompted us to divide the interscale in two regions (the interscale AP and the interscale LR) and quantify the proportion and orientation of clones in each region. At P30, around 70% of the clones were located in scale, 23% in interscale AP, and 7% in interscale LR (Figure 7A). In each region, around 70% of the clones were anisotropic (Figure 7B). Measuring the orientation of the anisotropic clones revealed a striking and complex pattern of clonal orientation, with interscale LR clones oriented perpendicularly to the long axis of the tail (Figure 7C), interscale AP clones elongated parallel to the long axis of the tail (Figure 7D), and scale clones with average angles between 40° and 80° (Figure 7E). Surprisingly, although the tail grows anisotropically in the AP direction, we found that the average orientation of all clones displayed little net anisotropic bias. This argued that the direction of cell division was decoupled with the direction of tissue growth in tail epidermis and raised the question of which local factor could influence cell division orientation

Previous studies highlighted the importance of the extracellular matrix and external forces on the orientation of cell division *in vitro* (Fink et al., 2011; Théry et al., 2005). To assess whether the collagen networks of the dermis could impose directional cues to clonal growth, we used bi-photon microscopy and second harmonic generation and analyzed the orientation of fibrillar collagen within the upper dermis in each IFE unit. At P30, a large-scale pattern in collagen was clearly visible, oriented in the AP direction in the AP interscale, the LR direction in the LR interscale, and at nearly 45° in the scale (Figures 7F–7H). Quantification of the orientation of the clones and orientation of collagen fibers revealed a strong correlation between the two (Figures 7I–7K). This spatial pattern perfectly matched the observed clonal orientation map, suggesting a functional link between the two. The strong correlation between collagen and clonal orientation was also found at earlier time points (Figures S7B and S7C).

To test whether the orientation of collagen fibers controls cell division orientation, we used photolithography-based micropatterning to engineer adhesive surfaces with aligned collagen fibers or a non-aligned collagen network, both with 2-μm spacing (Figure 7L; STAR Methods). We cultured primary keratinocytes on the two surfaces and scored the orientation of cell divisions under both conditions (Figure 7M). Interestingly, orientation of cell division correlated strongly with collagen fiber alignment, whereas the cell division plane was randomized on the non-aligned collagen network pattern (Figure 7N). Altogether, these data suggest that the spatial organization of the orientation of DPs is regulated by the local pattern of collagen fibers within the upper dermis during development.

DISCUSSION

In this study, we unraveled the clonal dynamics and the underlying mechanisms that mediate postnatal skin expansion using mouse tails and paw epidermis as models. By combining proliferation kinetics, quantitative clonal analysis, mathematical modeling, and single-cell RNA sequencing, we propose that postnatal expansion of the skin is mediated by single populations of DPs in the different skin regions that make stochastic fate choices at the single-cell level between division and differentiation are robustly imbalanced at the population level toward self-renewal. Our mathematical model reveals a surprising simplicity in the process of epidermal expansion. In particular, we find that quasi-linear epidermis growth is blueprinted via a combination of (1) a steadily decreasing cell division rate over time and (2) an intermediary level of imbalance between self-

Figure 6. Single-Cell RNA Sequencing of BCs in Young and Adult Tail Epidermis

(A and B) UMAP dimensionality reduction plots for the individual (left) P7 (A) and P60 (B) samples using Seurat and the integrated dataset (right) using Harmony. Colors represent cluster identities computed on the individual samples.

(C–O) Normalized expression of genes expressed in young (top panels) and adult (bottom panels). *Krt5* (C) highlights BCs. *Mcm7* (D), *Cdk1* (E), and *Cdc20* (F) are cell cycle genes revealing BCs in G1/S, S/G2/M, and late G2/M, respectively. *Ccnd2* (G), *Col17a1* (H), and *Sparc* (I) are three markers associated with stem/progenitor cells. *Sbsn* (J), *Krt1* (K), and *Krt36* (L) highlight all differentiated cells and differentiated cells in adult interscale and scale, respectively. *Sostdc1* (M) is highly expressed in population SC/CP G0 I in adult and DP G0 I in young samples; *Mt2* (N) and *Wnt4* (O) appear in DP G0 II together but in separated populations in adult samples.

(P) Slingshot lineage trajectories for non-cycling cells, showing a unique direction toward differentiated cells in young samples (top panel) and multiple directions toward interscale, scale, and SC/CP III cell populations (bottom panel).

See also Figure S6.

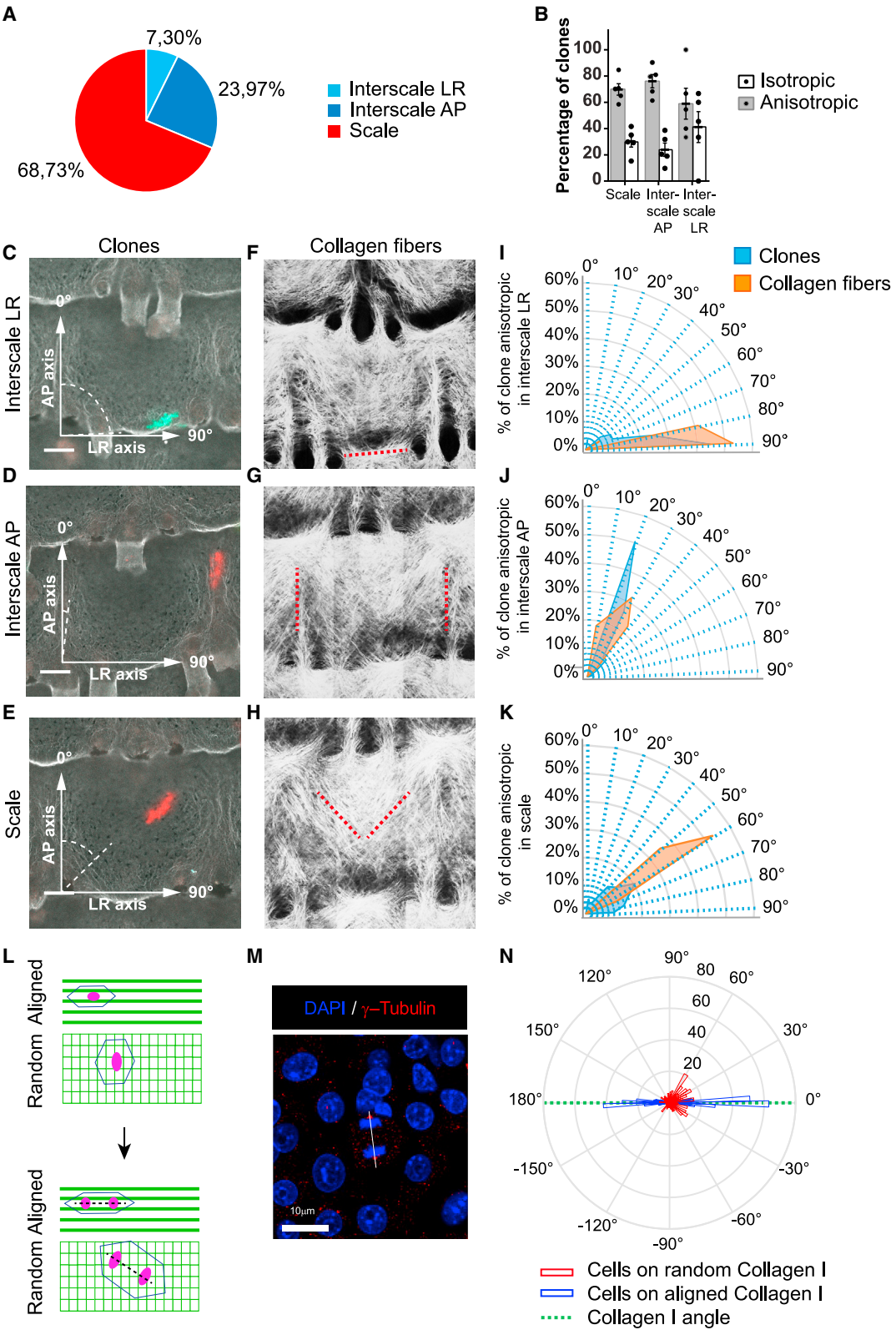

(legend on next page)

renewal and differentiation, which is nearly constant over time and even across tail scale and interscale regions.

We propose that the optimality during postnatal epidermal growth requires that the epithelium maintains a constant density of BCs throughout expansion and that the ratio of BCs to suprabasal cells is kept constant to ensure the barrier function of the skin, essential for animal survival. These two simple assumptions, which we validate experimentally, can only be fulfilled by a near-constant imbalance and ever-decreasing division rate, explaining qualitatively and quantitatively the design principles observed throughout epidermal postnatal growth. This suggests a model where cells regulate their fate choices not only to in-plane tissue expansion but also to constantly adjust the proportion of suprabasal cell produced to maintain epidermal thickness.

Our current model proposing a single population of DPs mediating tail growth in each scale and interscale region contrasts with the homeostatic model proposed previously, where more heterogeneous cell populations consisting of SCs and CPs have been proposed to co-exist in the interscale (Mascré et al., 2012; Sánchez-Danés et al., 2016). Different hypotheses can be advanced to explain this difference. The first would be that the IFE is only composed of DPs during postnatal development and that SCs and CPs derive from DPs after puberty. A second possible hypothesis would be that SCs are already present at birth but have similar dynamics as the CPs and only acquire their slow cycling dynamics later, between P30 and P60. Our single-cell RNA sequencing data suggest that IFE BCs are more homogeneous compared with adult BCs, which present an increase in heterogeneity with the appearance of an additional basal SC/CP population around P30 and two differentiated states corresponding to the scale and interscale differentiation program. The increase in BC heterogeneity coincided with the change in clonal dynamics, switching from an imbalance to a balance between renewal and differentiation, demonstrating that the clonal dynamics change around P30, at the end of postnatal growth.

Interestingly, the strong imbalance observed during postnatal development is highly similar to the one found during tumor initiation after oncogenic Hedgehog (HH) signaling (Sánchez-Danés et al., 2016) but strongly contrasts with the clonal dynamics reported upon wound healing (Aragona et al., 2017). Interestingly, similar to our results in postnatal development, the strong imbalance induced by the oncogene is constant over time and accompanied by a decreasing proliferation rate, leading to linear growth of the lesions over several weeks and months (Sánchez-Danés et al., 2016). In contrast, upon wounding, a strong increase in IFE BC proliferation occurs shortly after damage, but the basal clone size expands linearly, suggesting that wound healing is a much more rapid process that does not trigger an imbalance for self-renewal, instead relying on production of progenitors from activated SC populations (Aragona et al., 2017). Further experiments will be necessary to investigate the role of specific signaling pathways implicated in the control of cell fate decision.

Although we find epidermal expansion at the clonal level to be robustly coupled to expansion of the underlying tissue, analysis of clonal orientations demonstrated a more complex picture. Indeed, we found that the local orientation of cell division (and, consequently, clonal orientation) does not follow the axis of tail growth (which is overwhelmingly in the AP direction). Instead, clonal expansion is highly coupled to the local orientation of collagen fibers in the dermis, which display well-defined, long-range patterns throughout tail expansion. Using *in vitro* micropatterns of orientated or non-aligned collagen, we further demonstrated that the clonal orientation is dictated by the local pattern of collagen fibers. Interestingly, the observed patterns of collagen and clonal orientation (Figure 7) closely mirror those observed in *Drosophila* wing disc morphogenesis (Mao et al., 2013). In both systems, a central epithelial region (scale in our case) divides faster than its surroundings and displays radially oriented clones, whereas the surrounding regions (interscale in our case) display orthoradially oriented clones. Given that this pattern of orientation can be fully recapitulated *in silico* by a vertex model, where the enhanced proliferation of the central region mechanically compresses its surroundings (Mao et al., 2013), this suggests that similar mechanical competition could occur in our system between scale and interscale regions and provide a local orientation mechanism for clones. Further studies will be needed to understand how such intercalation events could be regulated as well as how global tissue expansion can scale with clone size while being uncoupled from local clonal orientation.

Altogether, our results suggest that postnatal epidermal expansion relies on tight and local regulation of three key parameters: cell fate imbalance, cell division rate, and orientation of cell division. Although some of these parameters could be partially determined by cell-intrinsic factors (where imbalance, for instance, could be programmed to match the expected tissue growth or division rate decaying autonomously in time), an alternative regulatory candidate would be cell-extrinsic cues, such as growth of the underlying dermis, epidermal thickness, cell density, and other mechanical constraints arising from the other epidermal cells and the external microenvironment (Andersen et al., 2019). This is consistent with recent findings regarding the role of nearest-neighbor interactions to couple basal division

Figure 7. The Orientation of Collagen Fibers Correlates with Clone Anisotropy and Tissue Expansion.

(A and B) Quantification of clone repartition (A) and the proportion of anisotropic and isotropic clones (B) counted on *K14-CreER/Rosa-Confetti* mice induced at P1 and analyzed at P30 (n = 726 clones from 5 mice). Error bars are mean ± SEM.

(C–F) Maximum-intensity projection of confocal images showing representative anisotropic clones in interscale LR (C), interscale AP (D), and scale (E) as well as a second harmonic signal highlighting fibrillary collagen in the upper dermis of the tail (F–H). Red dotted lines show fiber orientation. Scale bars, 100 μm.

(I–K) Quantification of anisotropic clone orientation and collagen fiber orientation relative to the AP axis in interscale LR (I), interscale AP (J), and scale (K).

(L–N) Schematic illustration (L) and quantification (M and N) of cell division orientation in primary keratinocyte 2D culture plated on collagen-coated micropatterned surfaces 24 h after seeding. Rose plots show the orientation angle with respect to aligned collagen fibers (0°). n > 300 mitoses/condition from 3 independent experiments; *p < 0.0001, Mann-Whitney test).

See also Figure S7.

and differentiation during epidermal homeostasis (Mesa et al., 2018; Miroshnikova et al., 2018; Rompolas et al., 2016), which provide a natural mechanism of BC density regulation. Such extrinsic mechanisms would be expected to increase the robustness of the model with respect to fluctuations, which is key, given that division rates and imbalances need to be tightly controlled in this system to achieve the correct size. Further experiments will be necessary to understand whether and how such feedback (tissue size, local density, thickness, division rate, and/or imbalance) is implemented mechanistically. Whether suprabasal density and/or tissue thickness are similarly regulated in other settings during development and homeostasis remains an intriguing question that will need to be explored in the future, as is the nature of the cross-talk between the epidermis and dermis that couples dermal and epidermal growth.

STAR★METHODS

Detailed methods are provided in the online version of this paper and include the following:

- KEY RESOURCES TABLE
- LEAD CONTACT AND MATERIALS AVAILABILITY
- EXPERIMENTAL MODEL AND SUBJECT DETAILS
  - Mice
- METHOD DETAILS
  - Monitoring epidermis growth
  - Quantification of Hair follicle, K31 and basal cell areas
  - Rosa-Confetti and Rosa-YFP clones induced in mice
  - Antibodies
  - Epidermal whole-mount and immunostaining
  - Whole skin clarification
  - Microscope image acquisition and measurements
  - EdU/Brdu proliferation experiments
  - H2BGFP proliferation experiments
  - FACS analysis of basal epidermal cells
  - Primary culture of keratinocytes
  - Quantification of EdU/BrdU experiments
  - Quantification and proliferation experiments on primary keratinocytes
  - Quantification of clone size and persistence
  - Quantification of the ratio suprabasal/ BCs and basal cell density in tail and paw epidermis
  - Quantification of clones and collagen fibers orientation
  - *In vitro* collagen I micro-patterning and quantification
  - Single cell RNA library preparation and sequencing
  - Single cell bio-informatic analysis
  - Theoretical modeling
- QUANTIFICATION AND STATISTICAL ANALYSIS
- DATA AND CODE AVAILABILITY

ACKNOWLEDGMENTS

The authors acknowledge the animal housing facility, the LiMiF microscopy platform, and the flow cytometry platform from ULB (Erasme campus). Sequencing was performed at the Brussels Interuniversity Genomics High Throughput core (http://www.brightcore.be) and the Genomics Core Leuven. The authors thank colleagues who provided reagents mentioned in the text, and J.-M. Vanderwinden and Michiel Martens for help with confocal imaging. S.D. is supported by a TELEVIE fellowship. M.A. is supported by a long-term fellowship from the HFSPO and a FNRS fellowship. A.S. and T.V. are supported by KULeuven (SymBioSys – C14/18/092), the Fondation Contre le Cancer (2015-143), and FWO postdoctoral fellowships 12W7318N and I001818N. S.A.W. is supported by the Helsinki Institute of Life Science, the Wihuri Research Institute, and Deutsche Forschungsgemeinschaft (DFG; project 73111208 – SFB 829). Y.A.M. has a Human Frontier Science Program fellowship (LT000861/2018). B.D.S. is supported by the Royal Society (EP Abraham research professorship RP\R1\180165) and the Wellcome Trust (098357/Z/12/Z). C.B. is an investigator with WELBIO and is supported by Fondation Contre le Cancer, the ULB Foundation, the Fond Gaston Ithier, Télévie, Foundation Bettencourt Schueller, Foundation Baillet Latour, and the European Research Council (EXPAND, ERC-2013-CoG number 616333).

AUTHOR CONTRIBUTIONS

S.D., E.H., B.D.S., and C.B. designed the experiments, performed data analysis, and wrote the manuscript. S.D., E.H., B.D.S., M.A., and C.B. discussed the data and their interpretation. S.D. performed most of the experiments. A.S., M.M., and T.V. performed single-cell RNA sequencing data analysis. Y.A.M. and S.A.W. performed micro-patterning experiments and data analysis. C.d.N., S.G., and C.D. provided technical support. E.H. and B.D.S. performed mathematical modeling and statistical analysis of the clonal data.

DECLARATION OF INTERESTS

The authors declare no competing interests.

Received: November 9, 2019
Revised: February 10, 2020
Accepted: March 5, 2020
Published: April 6, 2020

REFERENCES

Aibar, S., González-Blas, C.B., Moerman, T., Huynh-Thu, V.A., Imrichova, H., Hulselmans, G., Rambow, F., Marine, J.C., Geurts, P., Aerts, J., et al. (2017). SCENIC: single-cell regulatory network inference and clustering. Nat. Methods *14*, 1083–1086.

Andersen, M.S., Hannezo, E., Ulyanchenko, S., Estrach, S., Antoku, Y., Pisano, S., Boonekamp, K.E., Sendrup, S., Maimets, M., Pedersen, M.T., et al. (2019). Tracing the cellular dynamics of sebaceous gland development in normal and perturbed states. Nat. Cell Biol. *21*, 924–932.

Aragona, M., Dekoninck, S., Rulands, S., Lenglez, S., Mascré, G., Simons, B.D., and Blanpain, C. (2017). Defining stem cell dynamics and migration during wound healing in mouse skin epidermis. Nat. Commun. *8*, 14684.

Blanpain, C., and Fuchs, E. (2006). Epidermal stem cells of the skin. Annu. Rev. Cell Dev. Biol. *22*, 339–373.

Blanpain, C., and Simons, B.D. (2013). Unravelling stem cell dynamics by lineage tracing. Nat. Rev. Mol. Cell Biol. *14*, 489–502.

Boudaoud, A., Burian, A., Borowska-Wykret, D., Uyttewaal, M., Wrzalik, R., Kwiatkowska, D., and Hamant, O. (2014). FibrilTool, an ImageJ plug-in to quantify fibrillar structures in raw microscopy images. Nat. Protoc. *9*, 457–463.

Butler, A., Hoffman, P., Smibert, P., Papalexi, E., and Satija, R. (2018). Integrating single-cell transcriptomic data across different conditions, technologies, and species. Nat. Biotechnol. *36*, 411–420.

Clayton, E., Doupé, D.P., Klein, A.M., Winton, D.J., Simons, B.D., and Jones, P.H. (2007). A single type of progenitor cell maintains normal epidermis. Nature *446*, 185–189.

Diamond, I., Owolabi, T., Marco, M., Lam, C., and Glick, A. (2000). Conditional gene expression in the epidermis of transgenic mice using the tetracycline-regulated transactivators tTA and rTA linked to the keratin 5 promoter. J. Invest. Dermatol. *115*, 788–794.

Didierjean, L., Wrench, R., and Saurat, J.H. (1983). Expression of cytoplasmic antigens linked to orthokeratosis during the development of parakeratosis in newborn mouse tail epidermis. Differentiation *23*, 250–255.

Edgar, R., Domrachev, M., and Lash, A.E. (2002). Gene Expression Omnibus: NCBI gene expression and hybridization array data repository. Nucleic Acids Res. *30*, 207–210.

Fink, J., Carpi, N., Betz, T., Bétard, A., Chebah, M., Azioune, A., Bornens, M., Sykes, C., Fetler, L., Cuvelier, D., and Piel, M. (2011). External forces control mitotic spindle positioning. Nat. Cell Biol. *13*, 771–778.

Gomez, C., Chua, W., Miremadi, A., Quist, S., Headon, D.J., and Watt, F.M. (2013). The interfollicular epidermis of adult mouse tail comprises two distinct cell lineages that are differentially regulated by Wnt, Edaradd, and Lrig1. Stem Cell Reports *1*, 19–27.

Harris, T. (2002). The theory of branching processes (Courier Corporation).

Itzkovitz, S., Blat, I.C., Jacks, T., Clevers, H., and van Oudenaarden, A. (2012). Optimality in the development of intestinal crypts. Cell *148*, 608–619.

Jin, Y., Patel, P.H., Kohlmaier, A., Pavlovic, B., Zhang, C., and Edgar, B.A. (2017). Intestinal Stem Cell Pool Regulation in Drosophila. Stem Cell Reports *8*, 1479–1487.

Joost, S., Zeisel, A., Jacob, T., Sun, X., La Manno, G., Lönnerberg, P., Linnarsson, S., and Kasper, M. (2016). Single-Cell Transcriptomics Reveals that Differentiation and Spatial Signatures Shape Epidermal and Hair Follicle Heterogeneity. Cell Syst. *3*, 221–237.e9.

Klein, A.M., and Simons, B.D. (2011). Universal patterns of stem cell fate in cycling adult tissues. Development *138*, 3103–3111.

Korsunsky, I., Millard, N., Fan, J., Slowikowski, K., Zhang, F., Wei, K., Baglaenko, Y., Brenner, M., Loh, P.R., and Raychaudhuri, S. (2019). Fast, sensitive and accurate integration of single-cell data with Harmony. Nat. Methods *16*, 1289–1296.

Liu, N., Matsumura, H., Kato, T., Ichinose, S., Takada, A., Namiki, T., Asakawa, K., Morinaga, H., Mohri, Y., De Arcangelis, A., et al. (2019). Stem cell competition orchestrates skin homeostasis and ageing. Nature *568*, 344–350.

Livet, J., Weissman, T.A., Kang, H., Draft, R.W., Lu, J., Bennis, R.A., Sanes, J.R., and Lichtman, J.W. (2007). Transgenic strategies for combinatorial expression of fluorescent proteins in the nervous system. Nature *450*, 56–62.

Lun, A.T., McCarthy, D.J., and Marioni, J.C. (2016). A step-by-step workflow for low-level analysis of single-cell RNA-seq data with Bioconductor. F1000Res. *5*, 2122.

Mao, Y., Tournier, A.L., Hoppe, A., Kester, L., Thompson, B.J., and Tapon, N. (2013). Differential proliferation rates generate patterns of mechanical tension that orient tissue growth. EMBO J. *32*, 2790–2803.

Mascré, G., Dekoninck, S., Drogat, B., Youssef, K.K., Broheé, S., Sotiropoulou, P.A., Simons, B.D., and Blanpain, C. (2012). Distinct contribution of stem and progenitor cells to epidermal maintenance. Nature *489*, 257–262.

Mesa, K.R., Kawaguchi, K., Cockburn, K., Gonzalez, D., Boucher, J., Xin, T., Klein, A.M., and Greco, V. (2018). Homeostatic Epidermal Stem Cell Self-Renewal Is Driven by Local Differentiation. Cell Stem Cell *23*, 677–686.e4.

Miroshnikova, Y.A., Le, H.Q., Schneider, D., Thalheim, T., Rübsam, M., Bremicker, N., Polleux, J., Kamprad, N., Tarantola, M., Wang, I., et al. (2018). Adhesion forces and cortical tension couple cell proliferation and differentiation to drive epidermal stratification. Nat. Cell Biol. *20*, 69–80.

Mojtahedi, M., Skupin, A., Zhou, J., Castaño, I.G., Leong-Quong, R.Y., Chang, H., Trachana, K., Giuliani, A., and Huang, S. (2016). Cell Fate Decision as High-Dimensional Critical State Transition. PLoS Biol. *14*, e2000640.

Potten, C.S. (1975). Epidermal transit times. Br. J. Dermatol. *93*, 649–658.

Rompolas, P., Mesa, K.R., Kawaguchi, K., Park, S., Gonzalez, D., Brown, S., Boucher, J., Klein, A.M., and Greco, V. (2016). Spatiotemporal coordination of stem cell commitment during epidermal homeostasis. Science *352*, 1471–1474.

Sada, A., Jacob, F., Leung, E., Wang, S., White, B.S., Shalloway, D., and Tumbar, T. (2016). Defining the cellular lineage hierarchy in the interfollicular epidermis of adult skin. Nat. Cell Biol. *18*, 619–631.

Sánchez-Danés, A., Hannezo, E., Larsimont, J.C., Liagre, M., Youssef, K.K., Simons, B.D., and Blanpain, C. (2016). Defining the clonal dynamics leading to mouse skin tumour initiation. Nature *536*, 298–303.

Spearman, R.I., and Garretts, M. (1966). The effects of subcutaneous saline injections on growth and keratinization of mouse tail epidermis. J. Invest. Dermatol. *46*, 245–250.

Srinivas, S., Watanabe, T., Lin, C.S., William, C.M., Tanabe, Y., Jessell, T.M., and Costantini, F. (2001). Cre reporter strains produced by targeted insertion of EYFP and ECFP into the ROSA26 locus. BMC Dev. Biol. *1*, 4.

Street, K., Risso, D., Fletcher, R.B., Das, D., Ngai, J., Yosef, N., Purdom, E., and Dudoit, S. (2018). Slingshot: cell lineage and pseudotime inference for single-cell transcriptomics. BMC Genomics *19*, 477.

Susaki, E.A., Tainaka, K., Perrin, D., Kishino, F., Tawara, T., Watanabe, T.M., Yokoyama, C., Onoe, H., Eguchi, M., Yamaguchi, S., et al. (2014). Whole-brain imaging with single-cell resolution using chemical cocktails and computational analysis. Cell *157*, 726–739.

Théry, M., Racine, V., Pépin, A., Piel, M., Chen, Y., Sibarita, J.B., and Bornens, M. (2005). The extracellular matrix guides the orientation of the cell division axis. Nat. Cell Biol. *7*, 947–953.

Tian, H., Biehs, B., Warming, S., Leong, K.G., Rangell, L., Klein, O.D., and de Sauvage, F.J. (2011). A reserve stem cell population in small intestine renders Lgr5-positive cells dispensable. Nature *478*, 255–259.

Tobiasch, E., Winter, H., and Schweizer, J. (1992). Structural features and sites of expression of a new murine 65 kD and 48 kD hair-related keratin pair, associated with a special type of parakeratotic epithelial differentiation. Differentiation *50*, 163–178.

Tran, H.T.N., Ang, K.S., Chevrier, M., Zhang, X., Lee, N.Y.S., Goh, M., and Chen, J. (2020). A benchmark of batch-effect correction methods for single-cell RNA sequencing data. Genome Biol. *21*, 12.

Tumbar, T., Guasch, G., Greco, V., Blanpain, C., Lowry, W.E., Rendl, M., and Fuchs, E. (2004). Defining the epithelial stem cell niche in skin. Science *303*, 359–363.

Vasioukhin, V., Degenstein, L., Wise, B., and Fuchs, E. (1999). The magical touch: genome targeting in epidermal stem cells induced by tamoxifen application to mouse skin. Proc. Natl. Acad. Sci. USA *96*, 8551–8556.

Zhang, Y.V., Cheong, J., Ciapurin, N., McDermitt, D.J., and Tumbar, T. (2009). Distinct self-renewal and differentiation phases in the niche of infrequently dividing hair follicle stem cells. Cell Stem Cell *5*, 267–278.

Zheng, G.X., Terry, J.M., Belgrader, P., Ryvkin, P., Bent, Z.W., Wilson, R., Ziraldo, S.B., Wheeler, T.D., McDermott, G.P., Zhu, J., et al. (2017). Massively parallel digital transcriptional profiling of single cells. Nat. Commun. *8*, 14049.

Please cite this article in press as: Dekoninck et al., Defining the Design Principles of Skin Epidermis Postnatal Growth, Cell (2020), https://doi.org/10.1016/j.cell.2020.03.015

STAR★METHODS

KEY RESOURCES TABLE

REAGENT or RESOURCE	SOURCE	IDENTIFIER
Antibodies		
Chicken Polyclonal anti-K14	Thermo Fisher	Custom batch
Rat anti-integrin b4/CD104	BD Biosciences	Cat#553745, RRID: AB_395027
Guinea Pig polyclonal anti-acidic Hair Keratin K31	Progen	Cat# GP-hHA, RRID: AB_2716780
Rat anti-BrdU unconjugated	Abcam	Cat#Ab6326, RRID: AB_305426
Mouse Monoclonal anti-BrdU Alexa 647 conjugated	BD Biosciences	Cat#560209, RRID: AB_1645615
Mouse Monoclonal anti-BrdU (B44) FITC conjugated	BD Biosciences	Cat# 347583, RRID: AB_400327
Anti-rat Cy5 conjugated	Jackson Immuno Research	Cat# 112-175-167, RRID: AB_2338264
Anti-rat Alexa488 conjugated	Molecular Probes	Cat#A-21208, RRID: AB_141709
Anti-chicken Rhodamine Red-X conjugated	Jackson Immuno Research Lab	Cat# 703-295-155, RRID: AB_2340371
Anti-guinea pig Rhodamine Red-X conjugated	Jackson Immuno Research Lab	Cat# 706-295-148, RRID: AB_2340468
Anti-guinea pig Alexa488 conjugated	Molecular probes	Cat# A-11073, RRID: AB_2534117
Anti-CD34 Monoclonal antibody (RAM34), Biotin	Thermo Fisher Scientific	Cat# 13-0341-85, RRID: AB_466426
Anti-CD49f (integrin alpha 6)(GoH3), PE-conjugated	Thermo Fisher Scientific	Cat# 12-0495-81, RRID: AB_891478
Streptavidin, APC-conjugated	BD Bioscience	Cat# 554067, RRID: AB_10050396
Biological Samples		
Fetal Calf Serum	Merck Millipore	Cat# TMS-013-B
Rat tail Collagen I	Life Sciences	Cat# 354236
Human fibronectin	R&D Systems	Cat# 1918-FN
Chemicals, Peptides, and Recombinant Proteins		
Phalloidin Alexa488 conjugated	Life Technologies	Cat#A12379
Tamoxifen	Sigma	Cat# T5648
Doxycycline	Sigma	Cat# D9891
Urea	Merck Millipore	CAS 57-13-6, Cat# 1084881000
Sucrose	Merck Millipore	Cat# 107651
N,N,N',N'-tetrakis(2-hydroxypropyl) ethylenediamine	Tokyo Chemical Industry CO., LTD.,	Cat# T0781
Polyethylene glycol mono-p-isooctylphenyl ether/Triton X-100	Nacalai Tesque Inc	Cat# 25987-85
2,20,20'-nitrilotriethanol	Wako Pure Chemical Industries Ltd	Cat# 145-05605
7-Aminoactinomycin D (7-AAD)	Sigma	Cat# A9400
EdU (5-ethynyl-2′-deoxyuridine)	Invitrogen	Cat# A10044
BrdU (5-Bromo-2′-deoxyuridine)	Sigma Aldrich	Cat# B5002
HBSS	GIBCO	Cat#14170-88
Trypsin	GIBCO	Cat#15090-046
DMEM	GIBCO	Cat#41965-039
Chelex	Bio-Rad	Cat#142-2842
DPBS	Capricorn scientific	Cat# PBS-1A

(*Continued on next page*)

Continued

REAGENT or RESOURCE	SOURCE	IDENTIFIER
MEM	Sigma	Cat# M8167
Insulin	Sigma	Cat# I5500
EGF	Sigma	Cat# SRP3196
Transferrin	Sigma	Cat# T8158
Phosphoethanolamine	Sigma	Cat# P0503
Ethanolamine	Sigma	Cat# E0135
Hydrocortisone	Calbiochem	Cat# 386698
Glutamine	GIBCO	Cat# 25030-024
Penicillin-Streptomycin	GIBCO	Cat# 15070-063
Critical Commercial Assays		
Click-it EdU Imaging Kit	Invitrogen	Cat# C10339
FITC BrdU Flow kit	BD Biosciences	Cat# 559619
Chromium Single Cell 3′ microfluidic chips	10X Genomics	Cat# PN-120232
Chromium Single Cell 3′ Library Kit	10X Genomics	Cat# PN-120233
Deposited Data		
Single-Cell RNA sequencing data of this study	NCBI GEO	GEO: GSE146122
Experimental Models: Organisms/Strains		
Mouse: K14-CreER	Jackson Laboratory	Cat# 005107
Mouse: R26R-Confetti or R26R-Brainbow2.1	Jackson Laboratory	Cat# 013731
Mouse: Rosa26-YFP	Jackson Laboratory	Cat# 006148
Mouse: pTRE-H2BGFP	Jackson Laboratory	Cat# 005104
Mouse: K5-tTA	From Adam Glick	MGI:3575755
Mouse: $Lgr5^{DTR}$	Genentech	MGI:5294798
Mouse: CD1	Charles River	N/A
Software and Algorithms		
Zen software (2012)	Zeiss	N/A
CellRanger (version 3.0.2)	10X Genomics	https://support.10xgenomics.com/single-cell-gene-expression/software/pipelines/latest/installation
Scran R package (version 1.10.1)	Lun et al., 2016	https://bioconductor.org/packages/release/bioc/html/scran.html
Seurat R package (version 3.0.1)	Butler et al., 2018	N/A
Harmony R package (version 1.0)	Korsunsky et al., 2019	N/A
Slingshot R package (version 1.3.1)	Street et al., 2018	N/A
pySCENIC (version 0.9.19)	Aibar et al., 2017	https://scenic.aertslab.org/
AUCell R package (version 1.6.1)	Aibar et al., 2017	N/A
FibrilTool ImageJ plugin	Boudaoud et al., 2014	N/A
MATLAB software (vR2010a Student, Mathworks)	N/A	N/A

LEAD CONTACT AND MATERIALS AVAILABILITY

Further information and requests for resources and reagents should be directed to and will be fulfilled by the Lead Contact, Cedric Blanpain (cedric.blanpain@ulb.ac.be). This study did not generate new unique reagents.

EXPERIMENTAL MODEL AND SUBJECT DETAILS

Mice

K14-CreER (Vasioukhin et al., 1999) and *TRE-mCMV-H2B-GFP* (Tumbar et al., 2004) transgenic mice were provided by E. Fuchs. *K5tTA* (Diamond et al., 2000) mice were a kind gift from Glick. *Rosa-Confetti* (or *Brainbow-2.1*) mice (Livet et al., 2007) were provided by H. Clevers. *Rosa-YFP* (Srinivas et al., 2001) mice were purchased from Jackson Laboratory (USA). *Lgr5$^{DTR-EGFP}$* (used to exclude bulge *Lgr5+* cells) mice (Tian et al., 2011) were kindly provided by Genentech (San Fransisco, USA). CD1 mice were purchased from Charles River (France). Mice used in this study were composed of males and females with mixed genetic background and aged from 1 to 80 days. The exact age of the mice is specified in each experiments. The single-cell RNA sequencing was performed on males aged of 7, 30 and 68 days. No statistical methods were used to predetermine sample size. The experiments were not randomized. The investigators were not blinded to allocation during experiments and outcome assessment. Mice colonies were maintained in a certified animal facility in accordance with European guidelines. The experiments were approved by the local ethical committee (CEBEA) (#446N; #604N).

METHOD DETAILS

Monitoring epidermis growth

For the tail epidermis analysis (Figure 1), 3 mouse litters were used to measure the length (L) and width (W) (at the proximal part) of the tail every 1 to 3 day from P1 to P60 using a precision calliper. The surface (S) of the tail was calculated as a triangle with the formula $S = (W \times \pi \times L)/2$. For the hindpaw epidermis, pictures of whole-mount hindpaw were acquired entirely and the length (L) and the width (W) of the tissue were measured using the Zen software (n = 4 hinpaws per time point). The paw surface was calculated as a rectangular shape with the formula S = L x W.

Quantification of Hair follicle, K31 and basal cell areas

For Hair follicle and scale K31+ areas, measures were performed on maximum intensity projection of confocal pictures (10x objective) from whole-mount tissues stained with K31, β4 integrin and Hoechst. These data show that the epidermal region undergoing scale differentiation (K31+) arises around P7 at the center of the future scale region and is spreading rapidly until P14. After P14, the relative surface of the scale and interscale regions remains constant during the course of postnatal growth until adult homeostasis (Figures S1C and S1D). For K31+ area, a drawing line surrounding the surface was performed manually and the area was calculated using the ZEN2012 software. The HF area is defined as a rectangle surrounding the scale in which the width corresponds to the distance between two hair follicle lines in the antero-posterior axis (= Antero-Posterior (AP) distance) and the length corresponds to the distance between two central hair follicles located in adjacent triplets (= Left-Right (LR) distance). These distances were measured using the ZEN2012 software (Zeiss). The hair follicle (HF) area was calculated with this formula: HF = AP x LR. The average of four hair follicle units was calculated for each mouse for each time point ($n \geq 3$ mice per time point). To measure basal cell area, whole-mount tissues were stained with β4 integrin, phalloidin and Hoechst and pictures were acquired with the confocal microscope (40x objective, z = 1 μm). BCs were identified based on the orthogonal view and the expression of β4 integrin in their basal side. Cell area was measured manually by drawing the contour of each cell revealed by phalloidin signal in the x-y plan using the ZEN2012 software (Zeiss). The average area of 10 cells in scale and 10 cells in interscale was calculated per mouse (n = 3 mice per time point).

Rosa-Confetti and Rosa-YFP clones induced in mice

For lineage tracing experiment, *K14-CreER*/*Rosa-Confetti* mice were induced at postnatal day 1 (P1),P15 or P30 with Tamoxifen (0,01 mg/g diluted in 5%–10%vol/vol Ethanol and sunflower seed oil, Sigma cat. n° T5648) by intra-peritoneal (IP) injection. The same dose of tamoxifen was used to induce clones in both tail and paw epidermis. *K14-CreER*/*Rosa-YFP* mice were injected IP at P1 with Tamoxifen (0,001 mg/g). Mice were then sacrificed at the appropriate time points following injections.

Antibodies

The following primary antibodies were used: anti-Integrin β4/CD104 (rat, 1:200, BD Biosciences, 553745), anti-K14 (chicken, 1: 2000, custom batch, Thermo Fisher), anti-K31 (guinea pig, 1:400, Progen, GP-hHa1), anti-BrdU (rat, 1:200, Abcam), Alexa 647-coupled BrdU antibody (mouse, 1:200, BD Biosciences, 560209), anti-α6-integrin PE-conjugated (clone GoH3; 1:200, ebioscience) and biotinylated CD34 (clone RAM34; 1:50, BD Biosciences). The following secondary antibodies were used: anti-rat conjugated to Cy5 (Jackson Immuno Research) or to A488 (Molecular Probes), anti-chicken conjugated to Rhodamine Red-X (Jackson Immuno Research), anti-guinea pig conjugated to Rhodamine Red-X (Jackson Immuno Research) or to Alexa488 (Molecular Probes) and Streptavidin conjugated to APC (1:400, BD Biosciences). Alexa488 conjugated phalloidin (Life Technologies) was used 1:200 in blocking buffer to visualize F-actin microfilaments and highlight cell membranes. Nuclei were stained with Hoechst (1:2000).

Epidermal whole-mount and immunostaining

Pieces of skin from tail or hindpaw were incubated in PBS /EDTA (20mM) on a rocking plate at 37°C for 30 min (P1-P7 tail skin), 45 min (P15 tail skin) or 1 hour (P30, P60 tail skin and all hindpaw skin). Epidermis was separated from the dermis using forceps as an intact

sheet and washed 3 times with PBS. Pieces of epidermis were pre-fixed in 4% paraformaldehyde for 30 min to 1 hour at room temperature. Epidermis were rinsed 3 times with PBS for 5 min and conserved in PBS with 0.2% azide at 4°C. For immunofluorescence staining the entire pieces of epidermis were incubated in blocking buffer (1% BSA, 5% horse serum, 0.8% Triton in PBS) for 3 hours at room temperature on a rocking plate (100 rpm). The samples were incubated in primary antibodies overnight at room temperature, on the rocking plate (100rpm). Samples were then washed 3 times in PBS with 0.2% tween during 1 hour and incubated in appropriate secondary antibodies diluted 1:400 and Hoechst solution diluted 1:2000 in blocking buffer for 1-2 hour at room temperature on the rocking plate (100rpm). Then the samples were washed 3 times in PBS 0,2% tween and mounted in DAKO mounting medium supplemented with 2.5% Dabco (Sigma). For EdU/BrdU staining, samples were first stained with the primary antibody, washed and stained with the secondary antibody, following the protocol described above. Edu staining was performed following the manufacturer's instructions (Invitrogen). Briefly, the samples were blocked with a solution of BSA3% for 5min, permeabilized with a solution of Triton 0,8% for 20 min, blocked again with BSA3% for 5min and incubated in Click-it reaction Cocktail for 40 min in dark. The cocktail was removed and the samples were again blocked with BSA 3% for 5min, washed 3 times in PBS, fixed in PFA 4% for 10min and washed 3 times in PBS and incubated in HCl 1M at 37°C for 45 min. After, they were washed with PBS 0,2% Tween and incubated overnight with BrdU antibody in blocking buffer. The next day, samples were washed in PBS 0,2% Tween, incubated in Hoechst solution diluted 1:2000 in PBS 0,2% tween for 30 min. Samples were washed 3 times in PBS 0,2% Tween and mounted as described above.

Whole skin clarification

Whole skin (dermis and epidermis) was removed from the tail bone and fixed overnight in 4% PFA at 4°C. Samples were washed 3x in PBS and cleared using the Clear, Unobstructed Brain Imaging Cocktails and Computational analysis (CUBIC) described by Susaki et al. (2014). Briefly, ScaleCUBIC-1 (reagent 1) was prepared as a mixture of 25 wt% urea (Nacalai Tesque Inc., 35904-45, Japan), 25 wt% N,N,N',N'-tetrakis(2-hydroxypropyl) ethylenediamine (Tokyo Chemical Industry CO., LTD., T0781, Japan), and 15 wt% polyethylene glycol mono-p-isooctylphenyl ether/Triton X-100 (Nacalai Tesque Inc., 25987-85, Japan). ScaleCUBIC-2 (reagent 2) was prepared as a mixture of 50 wt% sucrose (Nacalai Tesque Inc., 30403-55, Japan), 25 wt% urea, 10 wt% 2,20,20'-nitrilotriethanol (Wako Pure Chemical Industries Ltd., 145-05605, Japan), and 0.1% (v/v) Triton X-100. Skin was cutted in pieces (1 to 2cm^2) and incubated in reagent 1 for 3 days on a rocking plate (100 rpm) at 37°C protected from the light, after which the solution was exchanged and the sample was washed with PBS several times at room temperature while gently shaking, immersed in 20% (w/v) sucrose (#107651, Merck) in PBS, degassed, and immersed in reagent 2 containing 7-AAD (1:1000, A9400, Sigma) for nuclei vizualisation, for 2 days at room temperature on a rocking plate. Each reagent were prepared freshly. Samples were acquired using 2-PE microscopy with the reagent 2 as immersion solution.

Microscope image acquisition and measurements

All confocal images from whole-mount epidermis were acquired at room temperature with a LSM780 confocal system fitted on an AxioExaminer Z1 upright microscope equipped with C-Apochromat 40x/1,1 water, Plan Apochromat 25x/0.8 water and C-Apochromat 10x/0.45 water immersion objectives (Zeiss, Iena, Germany). Optical sections (z = 2μm) 512 × 512 pixels were collected sequentially for each fluorochrome. Confetti colors were acquired using tracks (mCFP: Ex: 458 nm, Em: 464-518nm/ RFP: Ex: 543nm; Em: 570-625nm/ EYFP-nGFP: Ex: 488; Em: 508-571nm). For whole tissue representations of tail and paw, maximum intensity projections of confocal pictures were obtained with the ZEN2012 software. Second harmonic signal was acquired from cleared whole skin samples at room temperature with a LSM780 confocal system fitted on an AxioExaminer Z1 inverted microscope equipped with C-Apochromat 40x/1,1 immersion objective and a 2Photon laser Chameleon Vision II (690-1064nm) (Coherent) (Zeiss). Samples were excited at 920nm and acquired as z stacks (z = 4 μm). The datasets generated were merged and displayed with the ZEN2012 software (Zeiss). Pictures representing second harmonic signal are maximum intensity projections of several pictures over 40μm in the upper dermis.

EdU/Brdu proliferation experiments

For the double pulse experiments in the tail epidermis, mice were first injected IP with EdU (12,5mg/kg in PBS, Invitrogen) and second with BrdU (50mg/kg in PBS, Sigma). P4 and P7 CD1 mice were injected with one single injection IP of EdU and several injections (continuous pulse, 3 injections/day) of BrdU, 12h after the last EdU injection. Mice were sacrificed 24h and 48h after the first BrdU injection. P15 CD1 mice were injected IP with EdU (3 injections/day) and then injected IP with BrdU (3 injections/day) 12h after the last EdU injection. Mice were sacrificed 48h and 96h after the first BrdU injection. P30 and P60 CD1 mice were injected IP with EdU (3 injections/day) and then injected with BrdU (1 injection/ day) and BrdU was added in drinking water (1mg/ml). P30 and P60 CD1 mice were sacrificed 48h-96h and 96h-144h respectively after the first BrdU injection. For the BrdU experiments in the hindpaw, mice were injected with a single dose of BrdU (50mg/kg in PBS, Sigma) intraperitoneally and sacrificed 4 hours after.

H2BGFP proliferation experiments

K5tTA/TRE-mCMV-H2B-GFP mice were first treated with doxycycline (Sigma, cat n° D9891) by intraperitoneal injection (26mg/kg) at P1, P7, P21 or P30. Mice were continuously fed with doxycycline in drinking water (2g/L) (through their feeding mother for mice younger than P21) during one, two and for weeks until animal euthanasia. Samples were collected and analyzed by FACS.

FACS analysis of basal epidermal cells

The dermis and epidermis were removed from the tail bone using forceps. The samples were incubated in HBSS (GIBCO) 0,25% trypsin (GIBCO) at 4°C overnight. The next day, the epidermis was separated from the dermis. Epidermis was then incubated on a rocking plate (100 rpm) at room temperature for 5 min. BCs were mechanically separated from the epidermis by flushing 10 times under the epidermis. Tissues were then cut in small pieces with a scalpel and trypsin was neutralized by adding DMEM medium (GIBCO) supplemented with 2% Chelex Fetal Calf Serum (cFCS). Samples were filtrated on 70 and 40μm filter (Falcon). Cells were incubated in PBS 2% cFCS with primary antibodies for 30 min on ice, protected from the light, with shaking every 10 min. Basal IFE and upper hair follicle cells were stained using PE-conjugated anti-α6-integrin (clone GoH3; 1:200, ebioscience) and bulge cells were stained with biotinylated CD34 (clone RAM34; 1:50, BD Biosciences). Primary antibodies were washed with PBS 2% cFCS and cells incubated for 30 min in APC-conjugated streptavidin (BD Biosciences), on ice, with shaking every 10 min. Secondary antibody was washed with PBS 2% FCS and cells were incubated in Hoechst solution (1:4000 in PBS 2%cFCS) prior FACS analysis. Living epidermal cells were gated by forward scatter, side scatter and negative staining for Hoechst dye. For H2BGFP proliferation experiments, *K5tTA/TRE-mCMV-H2B-GFP* mice chased with doxycycline were used. BCs were targeted using CD34 negative and α6 integrin positive gating. For P7, P30 P60 basal epidermal cells sorting, $Lgr5^{DTR\text{-}EGFP}$ mice (Tian et al., 2011) (knockin mice containing an Enhanced Green Fluorescent Protein (EGFP) under the control of the *Lgr5* regulatory region, allowing to identify and exclude *Lgr5*-expressing cells of the bulge) were used and BCs of the interfollicular epidermis were enriched using EGFP negative, CD34 negative, α6 integrin positive gating. Analysis were performed on a FACS Fortessa (BD Bioscience) and using FACS Diva software. Cell sorting was performed using a BD Influx at KULeuven Core facility (Leuven, Belgium) (P7 and P60) or a FACS Aria I at the ULB Flow Cytometry platform (Brussels, Belgium) (P30).

Primary culture of keratinocytes

Primary tail keratinocytes were freshly isolated from mice aged of P2, P10, P30 and P60. Before isolation, the whole tail was washed 30sec in distilled water, 1min in 70% ethanol, 30 s in distilled water, 1 min in PBS and cleaned 5min in an antibiotic solution (Penicillin-Streptomycin diluted 200U in PBS). An incisional cut was performed along the long axis of the tail with a scalpel, the dermis and epidermis were separated from the tail bone and incubated (epidermis up) for 20min (P2) to 60 min (P60) in PBS 0,8% Trypsin (GIBCO) at 37°C on rocking plate. The epidermis was separated from the dermis and flushed 10x with a Pasteur pipette on the dermal side. The epidermis was cut in small pieces and trypsin was neutralized by adding Keratinocyte Growth Medium (KGM). KGM is composed of Minimum essential medium eagle (MEM, M8167, Sigma) complemented with Insulin (5μg/ml, I5500, Sigma), EGF (10ng/ml, SRP3196, Sigma), Transferrin (10μg/ml, T8158, Sigma), Phosphoethanolamine (10μM, P0503 Sigma), Ethanolamine (10μM, E0135, Sigma), hydrocortisone (0,36μg/ml, cat no 386698, Calbiochem), Glutamine (2mM, GIBCO), Penicillin (100U/ML), Streptomycin (100μg/ml, GIBCO), chelated fetal calf serum (cFCS, 10%, GIBCO) and CaCl2 (100μM). The cells were further dissociated with 5ml pipette up & down (15x). The cell solution was filtered through 70μm filter, centrifuged at 250xg for 10 min and resuspend in KGM. Viability was assessed by manual counting and Trypan blue. $1{,}5x10^5$ living cells were plated in 12 wells plates pre-coated with human fibronectin (10μg/ml) and rat tail collagen I (30μg/ml). The medium was changed after 24h to remove non-adhering cells.

Quantification of EdU/BrdU experiments

The quantification was made manually with the ZEN2012 software (Zeiss), using z stack acquisitions (z = 1-2μm, 40x objective) of wholemount tissues stained for K31, EdU and BrdU for the tail epidermis and for BrdU and K14 for the hindpaw epidermis. Nuclei were colored with Hoechst. For the tail epidermis analysis, a minimum of 300 basal EdU+ cells were counted per mouse for each time point in at least 4 HF units ($n \geq 3$ mice per time point). Given the slowing down of the division rate in time, we adapted the duration of the BrdU chase with developmental time (24h/48h for P4 and P7, 48h/96h for P15 and P30) in order to capture better dynamically the evolution of double labeling in time. For the hindpaw epidermis analysis, a minimum of 185 basal BrdU+ cells were counted per mouse for each time point (n = 3 mice per time point).

Quantification and proliferation experiments on primary keratinocytes

After 48h of culture, half of the medium was removed from each well containing primary keratinocytes and replaced by medium containing either BrdU (10μM final concentration) or fresh medium (control) for 2h. Cells were washed 3 times with PBS and incubated with Trypsin 0,25% and 0,5mM EDTA (GIBCO) for 20min at 37°C. Trypsin was neutralized with KGM containing serum, cells centrifuged (10min at 250 x g) and resuspend in PBS 2% cFCS for counting. 10^6 cells were stained for BrdU following the manufacturer's protocol (BD Bioscience). Briefly, cells were incubated with PE-conjugated anti-α6-integrin (clone GoH3; 1:200, ebioscience) diluted in PBS 2% cFCS for 30min on ice, with shaking every 10min. Cells were then washed with PBS 2% cFCS, centrifuged and the pellet was resuspended in Cytofix/Cytoperm. After an incubation of 15min at room temperature, cells were washed with Perm/Wash and centrifuged. Cells were then resuspended in Cytoperm Plus, incubated for 10 min on ice then washed with Perm/Wash and centrifuged. Cells were re-fixed with Cytofix/Cytoperm for 5 min at room temperature, washed with Permwash and centrifuged. Cells were then treated with DNase for 1h at 37°C, then washed with Perm/Wash and centrifuged. Finally, cells were resuspended in FITC-conjugated anti-BrdU (clone B44; 1:50, BD Biosciences) diluted in Perm/Wash and incubated 30 min at room temperature, then wash with Perm/Wash and centrifuged. Cells were finally resuspended in PBS 2% cFCS for FACS analysis. FITC positive cells were

quantified using the FACS Diva Software among the α6-integrin^{high} in two biological samples. At least 6000 living cells were analyzed for each experiment.

Quantification of clone size and persistence

For the tail epidermis analysis, regarding the absence of correlation between K31 staining and hair follicle area surface increase at early time points, we decided to not use the K31 staining to score the clones in scale but rather consider an elliptical surface covering 60% of the HF area at each time point (Figures S1A–S1C). Whole-mounts obtained from *K14-CreER*/*Rosa-Confetti* induced at P1,P15 or P30 and stained for β4 integrin were analyzed by confocal microscopy. Orthogonal view was used to see in 3 dimensions RFP, YFP, mCFP or nGFP positive cells and quantify the number of basal and total cells per clone. Cells were considered as basal when their basal side was positive for β4 integrin. For the tracing induced in the tail epidermis at P1, 104 clones at P4 (n = 3 mice), 158 clones at P7 (n = 4 mice), 245 clones at P15 (n = 5 mice), 295 clones at P30 (n = 5 mice) and 623 clones at P60 (n = 9 mice) were analyzed. For the tracing induced at P15, 178 clones at 4 days post-induction (n = 5 mice) and 286 clones at 2 weeks post-induction (n = 5mice) were analyzed. For the tracing induced at P30, 209 clones at 4 days (n = 5 mice) and 265 clones at 4 weeks (n = 5 mice) post induction were analyzed. For clonal persistence, large areas of tissue (at least 100 hair follicle triplets/mouse for P1 tracing, and 4 to 10 hair follicle triplets/mouse for P15 and P30 tracing) were scanned using the 10x or 25x objectives. The number of basally attached clones was divided by the number of hair follicle triplets counted in the same area ($n \geq 5$ mice per time point). For the hind-paw epidermis, clones were induced at P1 and were analyzed in the portion of the paw devoided of hair follicles and pads. 152 clones at P1 (n = 3 mice), 107 clones at P7 (n = 2 mice), 108 clones at P15 (n = 3 mice), 125 clones at P30 (n = 3 mice) and 80 clones at P60 (n = 3 mice) were analyzed. For the clonal persistence, the surface of the paw without hair follicles and pads was calculated on whole-mount using the Zen software and the total number of clones present within this area was counted.

Quantification of the ratio suprabasal/ BCs and basal cell density in tail and paw epidermis

Whole-mount tissues stained for β4 integrin, phalloidin and hoechst were acquired with confocal microscope (40x objective). BCs were positive for β4 integrin on their basal side. For the ratio of suprabasal/ BCs, the number of basal and suprabasal nuclei within a surface delimited in tail scale, tail interscale or paw were counted manually using the ZEN21012 software (Zeiss) for each time point. Suprabasal cells in the stratum corneum were not included. At least 230 BCs were counted per region per animal (n = 3 mice per time point).

Quantification of clones and collagen fibers orientation

To quantify clone orientation, whole-mount tissues stained with β4 integrin were acquired with confocal microscope (10x objective), files were processed with the ZEN2012 software (Zeiss) to obtain maximum intensity projection and were saved as *tiff.* files. 726 clones were manually scored as isotropic or anisotropic in *K14-CreER*/*Rosa-Confetti* (WT) (n = 5mice). Clone orientation was measured using Axiovision LE64 software (Zeiss) using the *Angle 3* measure tool, setting the 0° parallel to the antero-posterior direction of the Hair follicles. A total of 348, 131 and 29 anisotropic clones were measured in scale, interscale AP and interscale LR respectively, in *K14-CreER*/*Rosa-Confetti* (WT) mice (n = 5 mice). To quantify collagen fibers orientation, clarified whole pieces of skin from tail were acquired using 2-PE confocal microscopy. Z stack pictures representing second harmonic signal were merged as maximum intensity projections over 40μm in the upper dermis. Pictures were saved as *.tiff* files and quantification of the collagen fibers was made using the Fibriltool ImageJ plugin (for details, see Boudaoud et al., 2014). In brief, boxes were manually defined on large-scale 2D projections of the dermis, in each LR interscale, AP interscale and scale regions, and an average angle of orientation was extracted for each (defined as shown in Figure 7).

In vitro collagen I micro-patterning and quantification

Nikon TI-E inverted microscope (Nikon Instruments) equipped with a Super Plan FLuor 20x ELWD lens (Nikon) lens and a DMD-based UV (375nm) patterned PRIMO illumination device (Alveole) was used for all micropatterning experiments. PRIMO was controlled by the associated Leonardo plugin (V3.3, Alveole) on a micromanager platform (Fiji). In order to generate non-aligned mesh-like and aligned micropatterns, 2μm-spaced grids of either perpendicularly-intersecting or parallel lines, respectively, were projected onto plasma-treated (Corona Treater, ETP), PLLgPEG-passivated (SUSOS) 35mm glass-bottom dishes (Ibidi). Patterned areas were then conjugated with a uniform coating of collagen I by polymerizing 0.5mg/mL solution of rat tail collagen I (BS Bioscience) in 0.02N acetic acid over night at 4 degrees centigrade. The substrates were then washed with PBS, sterilized with 70% ethanol solution, and equilibrated with DMEM (GIBCO) prior to seeding 500K of freshly isolated E15.5 mouse keratinocytes onto each 35mm dish. Keratinocyte monolayers were allowed to proliferate on the patterns for 24 hours, at which time they were fixed and processed for immunofluorescence and quantification analyses. Division angles were quantified with respect to the directions of aligned collagen grids (set to 0 degrees) using γ-tubulin to mark the division axis. MATLAB software (vR2010a Student, Mathworks) was used to generate rose plots of angle distributions.

Single cell RNA library preparation and sequencing

After sorting, 6000 cells were loaded onto each channel of the Chromium Single Cell 3′ microfluidic chips (V2-chemistry, PN-120232, 10X Genomics) and individually barcoded with a 10X Chromium controller according to the manufacturer's recommendations

(10X Genomics). RNA from the barcoded cells was reverse transcribed, followed by amplification, shearing 5′ adaptor and sample index attachment. The libraries were prepared using the Chromium Single Cell 3′ Library Kit (V2-chemistry, PN-120233, 10X Genomics), quantified using a low coverage Illumina NextSeq 550 run and sequenced on an Illumina NovaSeq generating 343M, 245M and 336M reads for the P7, P30 and P60 libraries respectively. 10.338, 948 and 10.920 cells were detected, with a mean number of 33.179, 245.972 and 30.857 reads per cell, detecting a median of 2.290, 5.050 and 2.309 of genes per cell.

Single cell bio-informatic analysis

Sequencing reads were aligned and annotated with the mm10-1.2.0 reference dataset as provided by *10X Genomics* and demultiplexed using CellRanger (version 3.0.2) with default parameters. Cell-cycle assignment was performed using the *scran* R package (version 1.10.1) (Lun et al., 2016). Expression value scaling and normalization, PCA and UMAP dimensionality reductions and clustering were performed using the Seurat (Butler et al., 2018) R package (version 3.0.1). After filtering contaminant cells belonging to the infundibulum (*Sox9*^{high}, *Krt17*^{high}, *Krt79*^{high}) and sebaceous gland (*Scd1*^{high}, *Mgst1*^{high} and *Elovl6*^{high}) as well as cells containing a high content of mitochondrial genes, such as *mt-Co1* (dying cells) and filtering for cells with fewer than 2.500 UMI counts, 6.102, 673 and 7.551 cells were further analyzed in P7, P30 and P60 samples respectively. After filtering, expression values were renormalized, rescaled and re-clustered and cells were manually annotated based on their expression of differentiation related genes. A subset of clusters expressed cell-cycle related genes and were manually annotated considering the higher expression of known cell-cycle stage genes. Genes controlling DNA replication licensing (*Mcm2, Mcm3, Mcm7*) and DNA replication forks (*Lig1, Rpa2*) were used to define G1-S cluster (cluster 3 at P7 and P60). Genes controlling the entry in mitosis (*Top2a, Cdk1, Cenpf, Birc5, Cenpa, Ccnb2, Hmgb1*) were used to define the S-G2-M cluster (cluster 2 at P7 and cluster 4 at P60) which also had low expression of genes of the G1-S cluster (*Mcm2, Mcm3, Mcm7*). The Late G2-M cluster (cluster 4 at P7) harbored well known genes controlling mitosis (*Cenpa, Ccnb2, Hmgb1*) without the genes controlling G1-S (*Mcm2, Mcm3, Mcm7*) and lower expression of the genes controlling the entry of mitosis (*Top2a, Cdk1, Cenpf, Birc5*). Clusters were defined using Seurat at multiple resolutions (0.3, 0.5, 0.7, 0.9) and marker gene discovery was performed using the FindAllMarkers function of the Seurat package using the Wilcoxon Ranked Sum test. A clustering resolution of 0.5 was chosen as it resulted in the clearest set of transcriptional signatures and revealed clusters with biological significances, such as the differentiated cells in scale and interscale at P60. Markers were then selected by setting the threshold to all genes with an adjusted *p value* lower than 0.05. Pseudotime ordering of the IFE population was performed using the Slingshot R package (version (1.3.1) on the PCA embedding and the trajectories were visualized on the first 2 UMAP Components. Trajectory inference was performed on the datasets filtering out automatically annotated cycling cells and manually annotated cell-cycle related clusters.Gene regulatory network analysis was performed using pySCENIC (commit 0.9.9+2.gcaded79) (Aibar et al., 2017) with default parameters. AUC values for gene set enrichment were computed using the AUCell R package (version 1.6.1). Batch integration was performed using Harmony (version 1.0) after scaling expression values for each sample independently using Seurat.

Theoretical modeling

Theoretical basis for interpreting lineage tracing experiments

The theoretical basis of the lineage tracing data analysis in the mouse epidermis have been reviewed extensively in (Mascré et al., 2012; Sánchez-Danés et al., 2016), particularly in the context of homeostatic renewal and oncogenic activation. These studies have revealed that scale and interscale regions in the mouse tail epidermis consist of independent, stochastically renewing, populations: (i) a single population of progenitors in scale with perfectly balanced fate (dividing every 4-5 days); and (ii) a hierarchy of nearly-balanced, long-lived progenitors (also dividing every 4-5 days, and preferentially labeled in *Inv-CreER* mice), renewed infrequently by a rare population of stem cells (preferentially labeled in *K14-CreER* mice), undergoing stochastic fate choice, in the interscale. In order to clarify whether this hierarchy and spatial compartmentalization holds during postnatal development, a strategy of quantitative lineage tracing was implemented via the *K14-CreER* mouse tracing from P1 to P4, P7, P15, P30 and P60, to follow the dynamics of tail growth at the clonal level.

At all time points, clone size distributions, both for basal and suprabasal cells (resp. n_b and n_s), were found to be highly heterogeneous, and growing by a similar amount to the tail as a whole, arguing for clonal representativeness. We also found that scale clones were larger than interscale clones at all time points (see the "Quantification and Statistical Analysis" section). Strikingly, we found that basal clone size distributions at all time points converged toward a simple scaling form when rescaled by their average clone size $< n_b(t) >$, such that $P_{n_b}(t) = \frac{1}{< n_b(t) >} f\left(\frac{n_b}{< n_b(t) >}\right)$, and that this scaling form was consistent with a simple exponential size dependence, $f(n) = \exp(-n)$. Such an exponential scaling is expected to arise in the case of stochastic fate choices (i.e., a birth-death process) made by a single progenitor population. For instance, in the presence of a hierarchy of SCs and CPs both contributing significantly to the dynamics, clonal distributions should adopt more complex shapes which wouldn't show such scaling, as is observed upon oncogenic activation in mouse tail epidermis (Sánchez-Danés et al., 2016). We thus denote λ_s and λ_i respectively as the division rate of the progenitor population in scale and interscale. Upon each division, a progenitor P can give rise to three possible fate outcomes:

- $P \rightarrow P + P$ with probability $r + \Delta/2$
- $P \rightarrow P + D_b$ with probability 1-2 r
- $P \rightarrow D_b + D_b$ with probability $r - \Delta/2$

where r denotes the rate of symmetric over asymmetrical outcomes, and Δ the degree of imbalance between renewal and differentiation, which can be non-zero in a non-homeostatic condition. For reasons that will become clear, in the following sections, we take into account a differentiated basal intermediary D_b, which does not divide further and is committed to differentiation, with suprabasal stratification $D_b \rightarrow D_s$ taking place at rate Γ_1. Suprabasal cells do not divide and are shed at a rate Γ_2. Importantly, in the case of $\Delta = 0$, the theory predicts that, although the total labeled cell fraction should stay constant, the surviving clone size should increase linearly due to neutral drift (with a slope proportional to $r\lambda$), being compensated by a converse decrease in clonal persistence. The parameter r thus becomes crucial for the resulting dynamics. In contrast, in the presence of any amount of imbalance Δ, the persistence rapidly plateaus (Harris, 2002) while the clone size increases exponentially as $n_s(t) \propto \exp(\Delta\lambda t)$. Thus, the parameter r quickly becomes irrelevant to the resulting dynamics, and cannot be meaningfully constrained by our model fits. Indeed, as detailed below, Δ is large enough here to erase from the earliest time points the influence of r on clonal dynamics. We therefore concentrated on the imbalance Δ in this manuscript. We further note that, as in a developmental setting, all of the aforementioned parameters can be in principle time-dependent, drastically increasing the size of the parameter-space.

Theoretical basis for interpreting proliferation kinetics experiments

Because of the breadth of parameter space, we thus sought to constrain some parameters; in particular, the rates of division and differentiation over time. We thus turned to double-pulse EdU/BrdU experiments at all time points studied in the lineage tracing experiments, to both measure experimentally the rate of cell division in scale and interscale (by monitoring how quickly a cell that incorporated EdU will incorporate BrdU again), as well as the rate of basal to suprabasal transfer (by monitoring how quickly a cell that incorporated EdU will move to the suprabasal layers). The theoretical model used to fit the data was the same as that described in the section above, with three cell types considered (basal progenitor, basal differentiated and suprabasal differentiated). However, a small addition had to be made to the model, as we consistently observed that the processes of division and differentiation were not Poissonian: Instead, we found a refractory period after division, where a cell could neither divide again nor differentiate. This is consistent with findings from live-imaging studies of mouse epidermal homeostasis (Rompolas et al., 2016). We thus amended the model by considering that, for each process of division and differentiation, there was a latency period (respectively τ_{div} and τ_{diff}), followed by conventional stochastic (Poissonian) events. Such a two-phase model provided very good fits at all time points for both the fraction of double-labeled cells (Figure 3N) and the ratio of EdU suprabasal to BCs (Figure S2J) over time. We note, however, that such short-time correlations induced by refractory periods become quickly erased from the clonal data and, thus, for the lineage tracing experiments we used as inputs compound Poissonian rates defined by adding the two timescales (refractory and stochastic phases). These are shown as effective division rates in Figure 3O. Interestingly, we noted that the timescales of divison λ and suprabasal stratification Γ_1 were very similar in both compartments and across all time points. This is consistent with the basal layer being composed of a mixture of dividing progenitors and cells awaiting suprabasal stratification (in a roughly 1:1 ratio), matching with older observations (Potten, 1975). This is thus consistent with an extrinsic regulation of cell fate via near-neighbor couplings, as reported in homeostasis (Rompolas et al., 2016). The analysis also revealed consistently higher division and differentiation rates in scale throughout development, consistent with the increased clone size we observed in this region.

Fitting procedure and model validation

Once the division rate has been fixed by our proliferation kinetics experiments, we performed stochastic simulations of the model described in the subsection "Theoretical basis for interpreting lineage-tracing experiments." The initial condition for the numerical simulation is $n_b(0) = 1$ and $n_s(0) = 0$, mirroring the P1 clonal induction of single BCs. We perform at least 10,000 simulations for both scale and interscale, and calculate persistence, surviving clone sizes, and clone size distributions at all time points from these simulations (until P30, as growth drastically slows down after this time point). The only fitting parameters are Δ and r. We then performed a least-squares fitting procedure on the evolution of the mean basal clone size up to P30, to obtain optimal values of Δ and r in scale and interscale, as well as bootstrapping to build 95% confidence intervals on these parameters, following the same procedure as detailed in (Mascré et al., 2012; Sánchez-Danés et al., 2016). However, as mentioned above, r cannot be reliably fitted, given its low level of impact on the clonal dynamics. Indeed, trying to fit both Δ and r parameters from the basal clone size evolution yielded extremely large confidence intervals: $\Delta = 20\%^{+8\%}_{-8\%}$ and $r = 33\%^{+17\%}_{-20\%}$ in scale, and $\Delta = 24\%^{+4\%}_{-8\%}$ and $r = 21\%^{+15\%}_{-7\%}$ in interscale. Moreover, persistence could not be used either to meaningfully constrain the value of r, given its low effect on the dynamics, and the error bar involved in the measurements. As the values of r in both scale and interscale during development cannot be distinguished within these confidence intervals from its homeostatic values, we used these homeostatic values of $r \approx 0.2$ in the simulations.

In the following, we thus resorted to fitting procedure where Δ was the only fitting parameter. Importantly, we found that we could obtain very good fits to the mean basal clone size distribution with a single value of the fate imbalance (Figures 4A and 4D). As expected, the model reproduced well the exponential clone size distributions observed in the data at all time points (Figures 4B and 4E). We also found that the model could accurately predict the time evolution of the clonal persistence in both scale and interscale, characterized by an initial drop in persistence during the first week, followed by a near-plateauing behavior (Figures 4C and 4F). To probe further whether fate imbalance Δ could truly be considered as constant throughout development, we performed the same simulations and fitting procedure as before, but defining the imbalance Δ as a piece-wise function, which could take different inferred values Δ_1 (between P1 and P7), Δ_2 (between P7 and P15) and Δ_3 (between P15 and P30). This enabled us to test whether the fitting could be improved by inferring different values of imbalance over time, and thus test further the hypothesis of a near-constant inferred

imbalance. Importantly, this analysis confirmed that imbalance does not show a strongly varying temporal trend (neither in scale nor interscale), as shown on Figures 5G and 5H, although we cannot exclude small variations around the average imbalance, which would give rise to small variations of suprabasa/basal ratio.

Finally, to challenge the model further, we tested whether it could predict a fully independent set of data, performing clonal lineage tracing in the same mouse system, but inducing at P15 (and tracing for 4 days and 2 weeks). Importantly, we found that the model, as calibrated above (and thus in the absence of remaining free-parameters), provided a good prediction in scale and interscale, for both the time evolution of the surviving clone sizes (Figures 4R and 4S) and the clonal persistence (Figures 4T and 4U). This provided further support to the model, as well as to the assumption of a single progenitor population with near-constant imbalance in fate choice. After P30, the data on local and global tail expansion displays a transition phase toward a growth plateau, consistent with our observations at the clonal level (Figures 4B and 4E). We thus assumed that the system was abruptly transitioning toward homeostasis (Sánchez-Danés et al., 2016) after P30 (note that given the large clone size at P30, neither the evolution of clone sizes nor clonal persistence provided very strong constraints on the detailed dynamics), and used this as a guide for the eye (dashed lines in Figures 4B, 4C, 4E, and 4F). This assumption was further supported by our P30 tracing (Figure S5), which displayed results close to homeostasis (Sánchez-Danés et al., 2016).

Design principles of epidermal growth

As analysis of the lineage tracing data revealed a surprising degree of simplicity in the rules underlying tail epidermis expansion (nearly constant imbalance over time and across scale/interscale regions, while the division rate decreased steadily), we sought to understand the design principles underlying this phenomenology. To answer such a question, we resorted to a mean-field description of growth, forgetting about the stochasticity of cell fate choices, and writing conservation equations for the number of basal and suprabasal cells (b and s respectively):

$$\begin{cases} b'(t) = \lambda(t)\Delta(t)b(t) \\ s'(t) = \lambda(t)(1-\Delta(t))b(t) - \Gamma_2 b(t) \end{cases}$$

Here, we choose a loss rate for suprabasal cells proportional to basal cell number. This choice is rooted in the fact that suprabasal cells are not lost in "bulk," but instead are shed at the outer-most surface of the skin (which is thus proportional to the area of the skin surface). Note that because basal progenitors and basal differentiated cells have similar kinetics throughout development, we do not include at first the latter to give generic qualitative insights into the dynamics (although we will include it for quantitative matching to the results). As detailed below, as we impose the condition that basal cell number follows the growth of the underlying tissue, this results in this equation.

For mouse tail expansion, the epithelium is mechanically coupled to the growth of the underlying conjunctive tissue, which likely imposes its overall growth. A simple design principle for epidermal growth is thus, for BCs to maintain a constant density, so that their number evolution as a function of time is prescribed: $b(t) = b_0(t)$ a function which is imposed by the growth of underlying tissues. However, there are two unknown in the equation above, the division rate $\lambda(t)$ and the imbalance $\Delta(t)$, so that $b(t) = b_0(t)$ only imposes a relationship between the two. Thus, this could be both achieved via constant imbalance and varying division rate, or vice versa. A second design/principle must thus be enforced, and we review several possibilities below (Figures 5A–5D):

- Maintaining a constant number of progenitors $(\Delta = 0)$ (Figure 5A). This case would correspond to settings where the stem cell/progenitor pool is fixed and non-plastic (as observed for instance in experiments depleting the stem cell pool in *Drosophila* midgut (Jin et al., 2017). In this case, a third species (basal differentiated cells) must be taken into account to increase basal cell numbers, and the concentration of basal progenitors would get depleted in time as more and more differentiated BCs populate the basal layer to keep up with the growth of the underlying tissue. This is not what is observed in our data, and is also inconsistent with adult homeostasis of the tail epidermis (Mascré et al., 2012; Sánchez-Danés et al., 2016).
- Minimizing the total number of basal divisions (for instance to minimize the time to build up a population), corresponding to a so-called "bang-bang" dynamics as studied for the growth of intestinal crypts (Itzkovitz et al., 2012; Figure 5B). In this case, the solution is a phase of purely symmetric division $(\Delta = 100\%)$ to build-up progenitor cell numbers, followed by differentiated cell production. However, this results in a depletion of the density of suprabasal cells during the primary phase (not observed *in vivo*, see Figure 5E), and is not consistent with our lineage tracing dataset either showing that suprabasal cells are produced after birth (Compare the average number of basal and total cells at P4 in Figures 2E and 2F).
- Maintaining a constant division rate λ_p (Figure 5C).In this case, the imbalance must constantly adapt to fuel basal expansion, and can be expressed simply as $\Delta(t) = b_0'(t)/\lambda_p/b_0(t)$. One should note that this puts some constraints on growth (or division), as the imbalance can never be larger than 1; although this can be implemented in the realistic growth coefficients measured here. However, this scenario (which is not supported by our cell proliferation kinetics) would then predict a changing (and typically non-monotonous) evolution of suprabasal clones sizes (as the imbalance is too high initially to produce enough suprabasal cells, and too large afterward).
- Finally, a fourth possibility is that the epithelium needs to maintain a given suprabasal cell number as well $s(t) = s_0(t)$ (which means that even in the absence of suprabasal loss, a precise number of suprabasal cell must be produced to keep up with area expansion) (Figure 5D). We measured the time evolution of basal and suprabasal cell concentrations in both scale and

interscale, and found that this assumption was well-supported by the data. We thus explore its consequences for the regulation of division rate and imbalance during post-natal growth.

In the general case, this fourth constraint (prescribed evolution of basal and suprabasal densities) leads to

$$\begin{cases} \Delta(t) = \dfrac{1}{1 + \lambda b'/b + s'/b'} \\ \lambda(t) = \Gamma_2 + \dfrac{b' + s'}{b} \end{cases}$$

where the division rate needs to match the loss rate, in addition to a part of the growth burden. Furthermore, in the case where the epithelium seeks to maintain an identical ratio of basal to suprabasal cell $s_0(t)/b_0(t) = K$, (which is also supported by our data, see Figure 5E), the equation simplifies to

$$\begin{cases} \Delta(t) = \dfrac{1}{1 + K + \Gamma_2\, b'/b} \\ \lambda(t) = \Gamma_2 + \dfrac{b' + s'}{b} \end{cases}$$

In the limit of negligible suprabasal cell loss Γ_2, the imbalance Δ generically becomes a time-independent constant, for any temporal evolution of tail growth $b_0(t)$. This fitted well our findings, where we found the imbalance not only to be almost constant in time, but also constant in scale and interscale, even though both compartments grow at different rates.

To go beyond such qualitative arguments, we then incorporated the fact that tail growth is nearly linear ($b(t) = 1 + \alpha t$, where $\alpha \approx 0.3 d^{-1}$ for interscale and $\alpha \approx 0.6 d^{-1}$ for scale, based on Figure 1), used the experimentally measured ratio of basal to suprabasal cells, $K = 0.8$, and included differentiated BCs in the descriptions (with the constraint of 1:1 ratios with BCs throughout development). This yields a modified, but qualitatively similar expression:

$$\begin{cases} \Delta(t) = \dfrac{1/2}{1 + K + \Gamma_2/(1/\alpha + t)} \\ \lambda(t) = 2\dfrac{(1+K)\alpha + \Gamma_2(1+\alpha t)}{2 + \alpha t} \end{cases}$$

where, again, in the limit of negligible suprabasal loss, one predicts a constant imbalance and time-varying division rate. Quantitatively, applying this simple theory with the measured K ratio predicts $\Delta = 27\%$ in close agreement to the experimentally inferred value from lineage tracing ($\Delta = 24\%$). More quantitatively, we found that performing a joint fitting for $\Delta(t)$ and $\lambda(t)$ revealed that a loss rate of $\Gamma_2 \approx 0.04 d^{-1}$ provided good fits for the time evolution of the division rates and imbalance. In Figures 5G and 5H, we show this, plotting the inferred imbalance when fitted as piece-wise function (see section "Fitting procedure and model validation"), to emphasize the lack of strong temporal variation in imbalance compared to division. Strikingly, the model predicted that the twice-faster growth of the scale region should dominantly translate into a consistently higher division rate in scale, in qualitative and quantitative agreement with the data (Figures 3O and 3P). This argues that the evolution of both the division rate and the fate choices of DPs can be predicted quantitatively via the simple design principle of uniform basal and suprabasal growth (and is, in fact, the only scenario consistent with this principle).

To further demonstrate how large deviations from our paradigm would produce different predictions on observable data such as the evolution of the basal density and suprabasal/basal ratio, we also performed a sensitivity analysis (Figures S4A–S4D). We explored in particular: i) the influence of the value of constant imbalance Δ (with continually adjusting division rate), showing for instance that imbalances of 15% or 40% produce highly different predictions, poorly fitting the data (which is due to the fact that unbalanced dynamics constitutes an exponential process, highly sensitive to variations in growth rate; Figure S4A), ii) the predictions of bang-bang dynamics (transition from Δ = 100% to 0% imbalance at varying time points) together with a continually decreasing division rate, showing a very poor fit to the data, in particular as it produces a vast excess of BCs (Figure S4B), iii) the prediction of a "soft" bang-bang dynamics (transition from varying, partial imbalance values Δ to 0% imbalance at P15), which again provides poor fits to the data, in particular as it predict a drop of basal density post P15, not observed in the data (Figure S4C), and iv) a continually adjusting/decreasing imbalance, together with a constant division rate, although we show with independent proliferation experiments that this is not the case in the mouse epidermis (shown in Figure S4D for 1,2,3 and 4 divisions per week).

Extension to the morphogenesis of the neonatal paw epidermis

Finally, we sought to test whether a similar paradigm could be found in other tissues, such as the paw epidermis. Neonatal paw epidermis expanded 6-fold between P1 and P60, with most of the growth occurring between P1 and P15 (4.5-fold; Figure S3D). Rescaled clone size distributions at all time points fitted well with a single exponential (Figure S3L), as in scale and interscale of the tail epidermis, so we fitted the clonal data to the same model of a single population undergoing stochastic fate choices as described in the above paragraphs. Proliferation kinetics were inferred via short pulses of Brdu and measuring the fraction of Brdu+ cells in the

basal layer at P4, P7, P15, P30 and P60 (Figures S3E and S3F). To convert this information into division rate, we used the live-imaging data of Rompolas et al. (2016) in paw homeostasis to estimate the division rate of BCs at P60, and used this calibration to proportionately estimate the division rates at the other time points (shown in Figure S3N). Then, we estimated as before the fate choice parameters of BCs between P1 and P15 as $\Delta = 20\%$, which provided good fits for the time evolution of the basal clone size (Figure S3M) and clonal persistence (Figure S3O). Based on the overall dynamics of paw growth, we assumed that imbalance was zero around P18 (sharp transition to homeostasis), which fitted well the subsequent P30 and P60 time points (Figure S3M), although our time resolution cannot distinguish sharp versus smooth transitions to homeostasis. As this provided a good fit to the data, this argues again that neonatal growth in paw is well described by a model of near-constant fate imbalance toward symmetric division, with a constantly decreasing division rate. Based on our optimality theory, and given the measurements in paw of growth speed of $\alpha \approx 0.3\, d^{-1}$ (very similar to the growth speed of the interscale in tail epidermis) and suprabasal to basal ratio of $K \approx 1.2$ (slightly highly than in tail epidermis), we would predict (in the simplified case without loss) that $\Delta = 24\%$ which is thus again in good agreement with the experimental findings.

QUANTIFICATION AND STATISTICAL ANALYSIS

Quantification of clone sizes were performed on whole-mount tissue acquired by confocal microscopy and counted manually using the ZEN2012 software.

To test whether scale and interscale clone size distributions were significantly different, we compared the basal clone sizes of each of them, using the Mann-Whitney non-parametric test (as distributions were exponential and didn't pass a normality test). We found significant differences at all time points (P7: $p = 0.007$, P15: $p < 0.0001$, P30: $p < 0.0001$, P60: $p < 0.0001$), with interscale clones being consistently smaller. This could not be explained by a conversely higher suprabasal clone size in interscale, as scale suprabasal clones were also consistently and significantly larger, again assessed via a Mann-Whitney test (P7: $p = 0.028$, P15: $p < 0.0001$, P30: $p < 0.0001$, P60: $p < 0.0001$).

DATA AND CODE AVAILABILITY

The single-cell RNA sequencing data discussed in this publication have been deposited in NCBI's Gene Expression Omnibus (Edgar et al., 2002) and are accessible through GEO Series accession number GEO: GSE146122 (https://www.ncbi.nlm.nih.gov/geo/query/acc.cgi?acc=GSE146122).

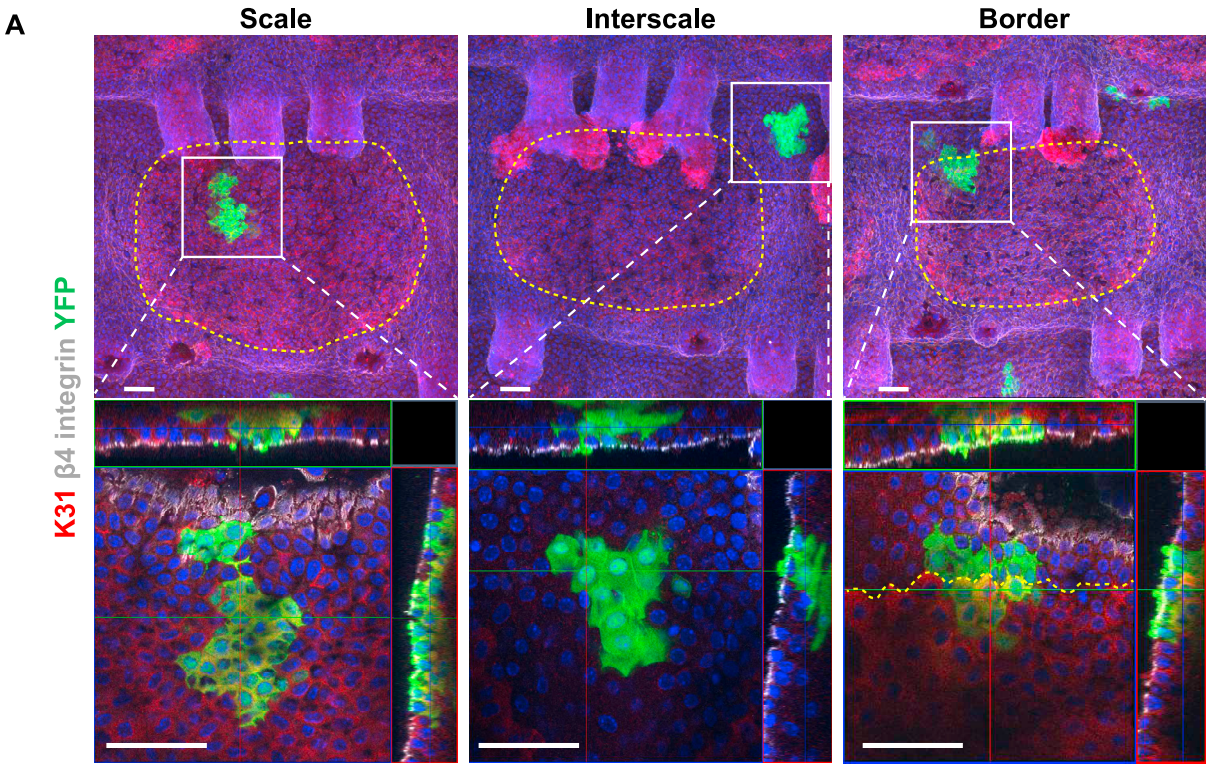

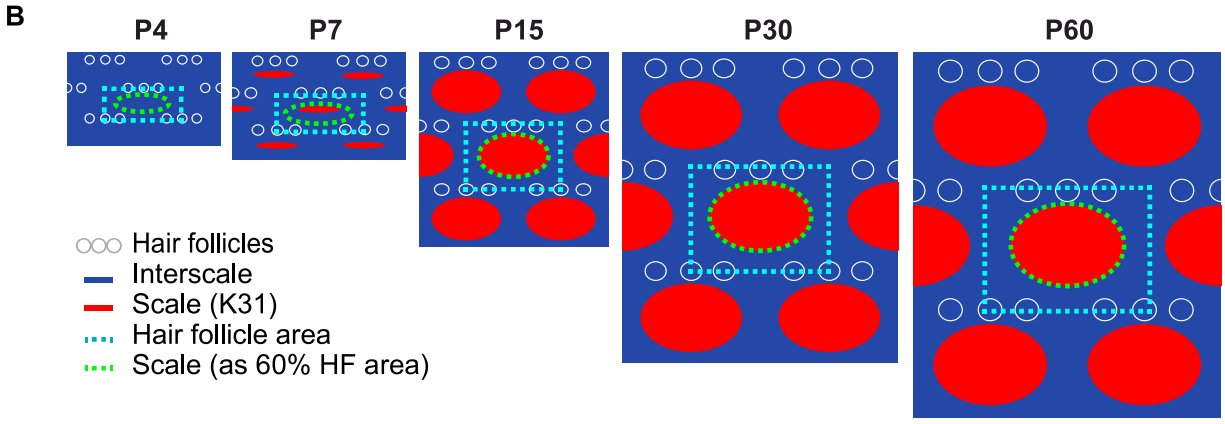

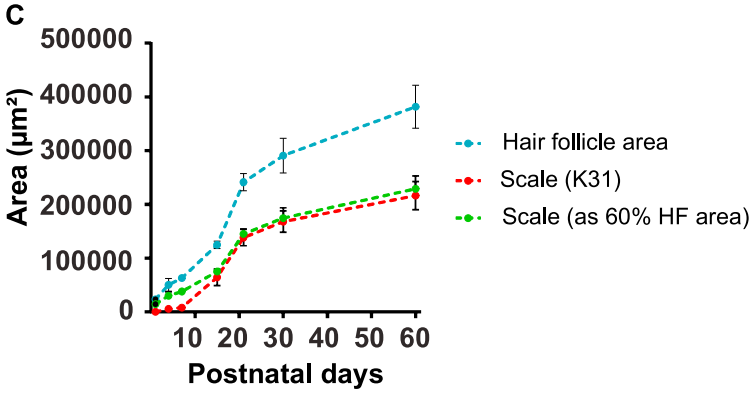

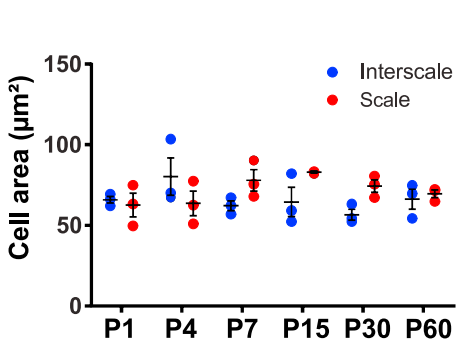

(legend on next page)

Figure S1. The HF Area Expands Linearly during Postnatal Development, Related to Figure 1

(A) Maximum intensity projection (upper panels) and confocal images (lower panels) of *K14-CreER*/*Rosa-YFP* clones induced at P1 showing that clones appear in the scale (left), interscale (middle) and also at the border of the two regions (right) at P30. These data show that scale and interscale compartments are not yet defined at the time of the tracing induction. Yellow dotted line surround scale region. Nuclei are stained with Hoechst. Scale bar = 50μm. (B-C) Schematic (B) and measurement (C) of the surface area occupied by suprabasal cells expressing K31 compared to the hair follicle area measured by the HF coordinates as 60% of the HF area. Our measures show that the HF area grows 2-fold from P7 to P15 while K31 staining expands 8-fold, suggesting that a change in K31 expression occurs in the suprabasal cells that is not the reflection of cell division as no particular increased cell division in the scale region reflects this expansion. The expansion of K31 area correlates well with the overall tissue growth only after P15, when scale and differentiation is complete. Data are represented as mean ± SEM ($n \geq 3$ mice per time point). (D) Surface area of the scale and interscale BCs at different time points, measured on confocal pictures, showing no difference of cell size during postnatal development (See STAR Methods). Data are represented as mean ± SEM (n = 3 mice per time point).

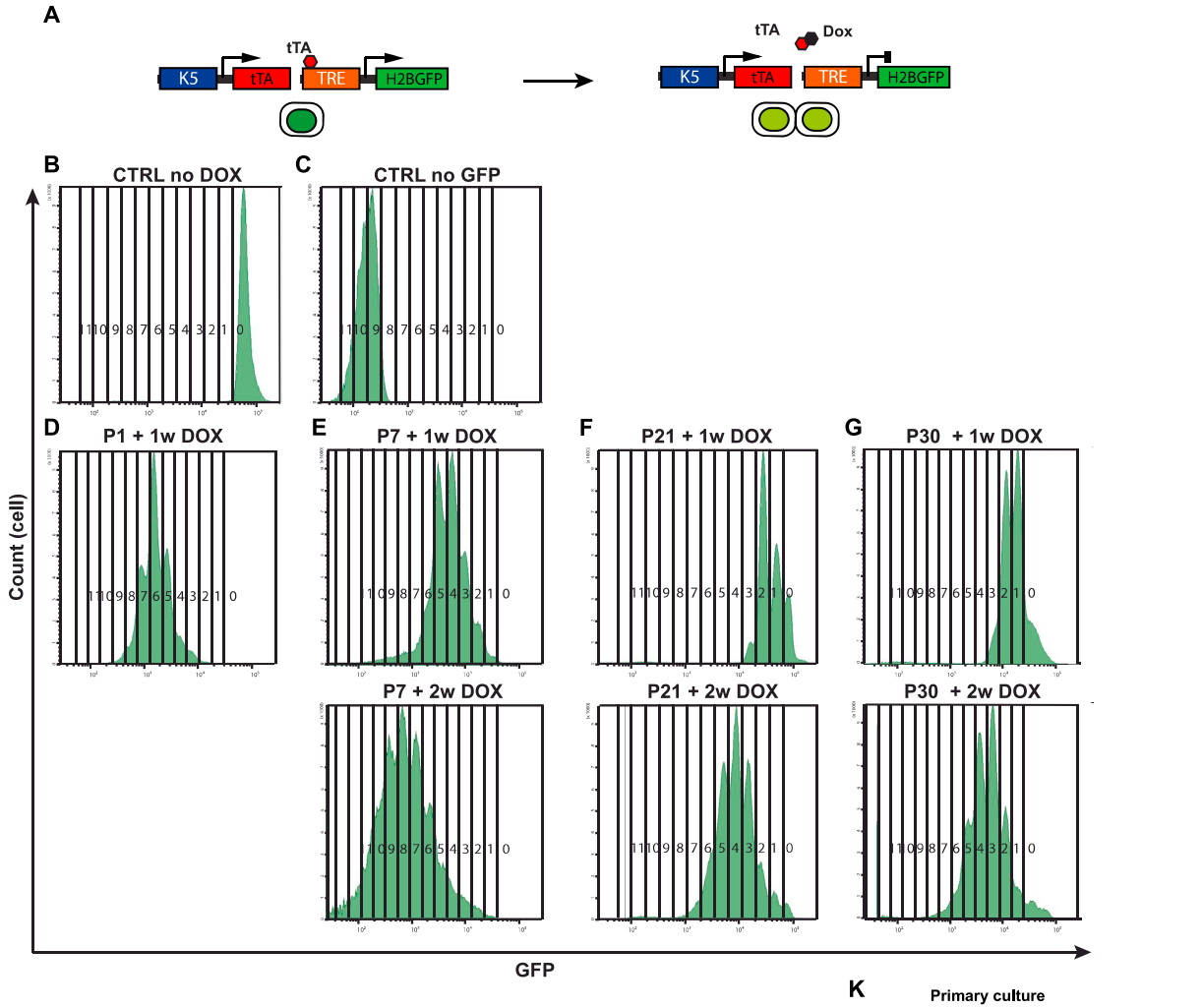

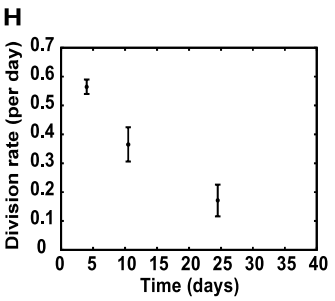

I

Time point	Tdiv (days)	SD
P1-P7	1,23	0,05
P7-P15	1,90	0,31
P21-P28	4,05	1,30

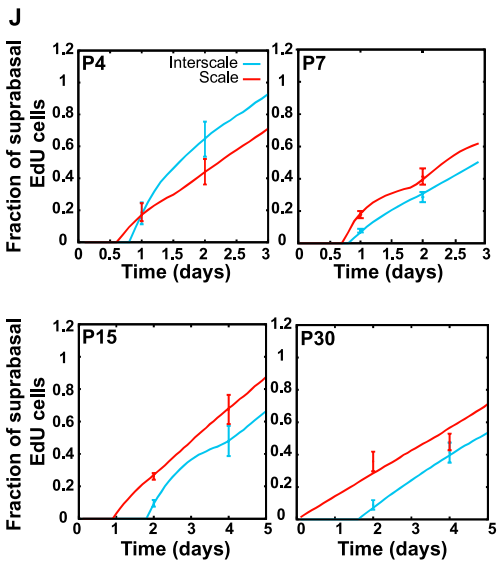

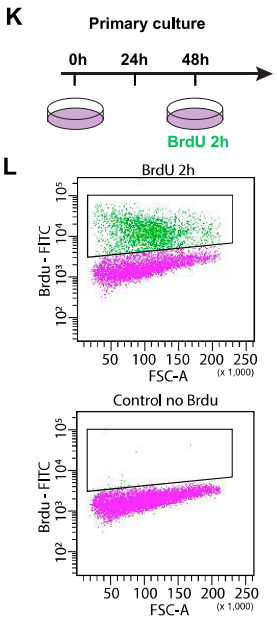

(legend on next page)

Figure S2. Ever-Decreasing Proliferation Rate of DPs during Postnatal Growth, Related to Figure 3

(A) Genetic strategy used to induce H2B-GFP pulse chase experiments in epidermal BCs and monitor the number of basal cell division overtime. In the absence of doxycycline (Dox) in *K5tTA/TetO-H2B-GFP* mice, H2B-GFP is expressed at a uniform and high level in all BCs. Upon Dox addition, the transcription of H2BGFP is blocked and H2B-GFP fluorescence is diluted by 2 at each cell division, which can be quantitatively monitored by FACS. (B-G) Examples of H2B-GFP fluorescence peak patterns observed in Itga6^{high} CD34^{negative} by FACS analysis in unchased mice having a high intensity of H2B-GFP (B), control CD1 mouse without any GFP signal (C), P1 mice after one week of chase (D), P7 (E), P21 (F) and P30 (G) mice with different chase periods, n = 3 mice per time point. (H-I) Calculated division rate of BCs over time from the distribution of the H2B-GFP dilution after 1 week (H) and average division time (Tdiv) of epidermal BCs for each mouse age inferred from H2B-GFP analysis (I). Data are represented as mean ± SD. (J) Fraction of suprabasal EdU+ cells over basal EdU+ cells in scale and interscale in EdU/BrdU double labeling experiments at different time points (see STAR Methods). n ≥ 3 mice per time point. Data are represented as mean ± SD. Dots, experimental data; lines, model prediction (K-L) Scheme (K) and representative FACS plot (L) of primary culture experiment used to asses the proliferation rate of freshly isolated keratinocytes. Primary cells isolated from tail mice aged of P2,P10, P30 and P60 were cultured for 48h, treated for 2h with BrdU and collected for FACS analysis. Untreated cells were used as negative control.

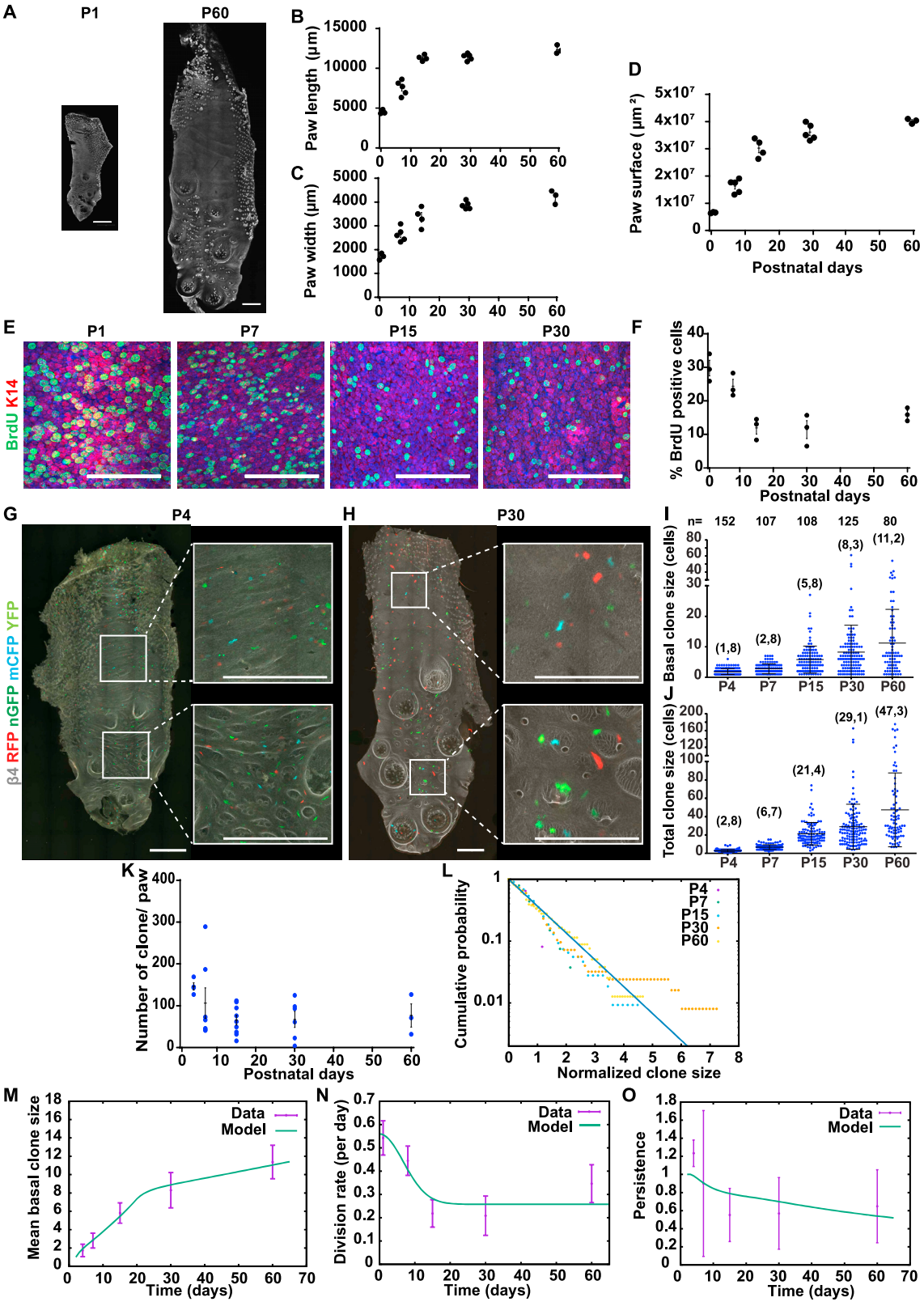

(legend on next page)

Figure S3. Lineage Tracing of DPs in the Paw Epidermis Also Recapitulates Tissue Expansion, Related to Figure 4

(A) Whole-mount paw epidermis from newborn (P1) and adult (P60) mice. (B) Measurement of the length of the paw from P1 to P60 ($n \geq 5$ mice). (C) Measurement of the paw width from P1 to P60 ($n \geq 5$ mice). (E) Calculated total paw surface showing a linear increase from P1 to P15 reaching a plateau after P21 ($n \geq 5$ mice). (E-F) Whole-mount paw epidermis (E) and quantification of BrdU positive BCs (F) analyzed in P1, P7, P15 and P30 epidermis 4h after a pulse of BrdU. (G-H) Representative pictures of whole-mount paw epidermis from *K14-CreER*/*Rosa-Confetti* mice induced with 10μg of Tamoxifen at P1 and collected at P4 (G) and P30 (H). Scale bar = 1mm. (I-J) Quantification of the number of basal (I) and total (J) cells per clone in paw epidermis counted on confocal pictures from P4 to P60 and showing the expansion of the clones over time. N: number of analyzed clones, brackets: average clone size. (K) Quantification of the number of clone per paw epidermis overtime. (L) Cumulative distributions of paw basal clone size, rescaled by average clone size at all time points (purple, green, blue, orange and yellow dots resp. for P4, P7, P15, P30 and P60). In all cases, the rescaled distributions are well-described by a simple exponential distribution (black line). Data are represented as mean ± SEM (M-O) The theoretical model predicts well the experimental measures of the basal clone size expansion (M), the decreasing proliferation rate (N) and the clonal persistence (O) in the paw epidermis. Symbols, experimental data; green lines, model predictions. Data are represented as mean ± SEM.

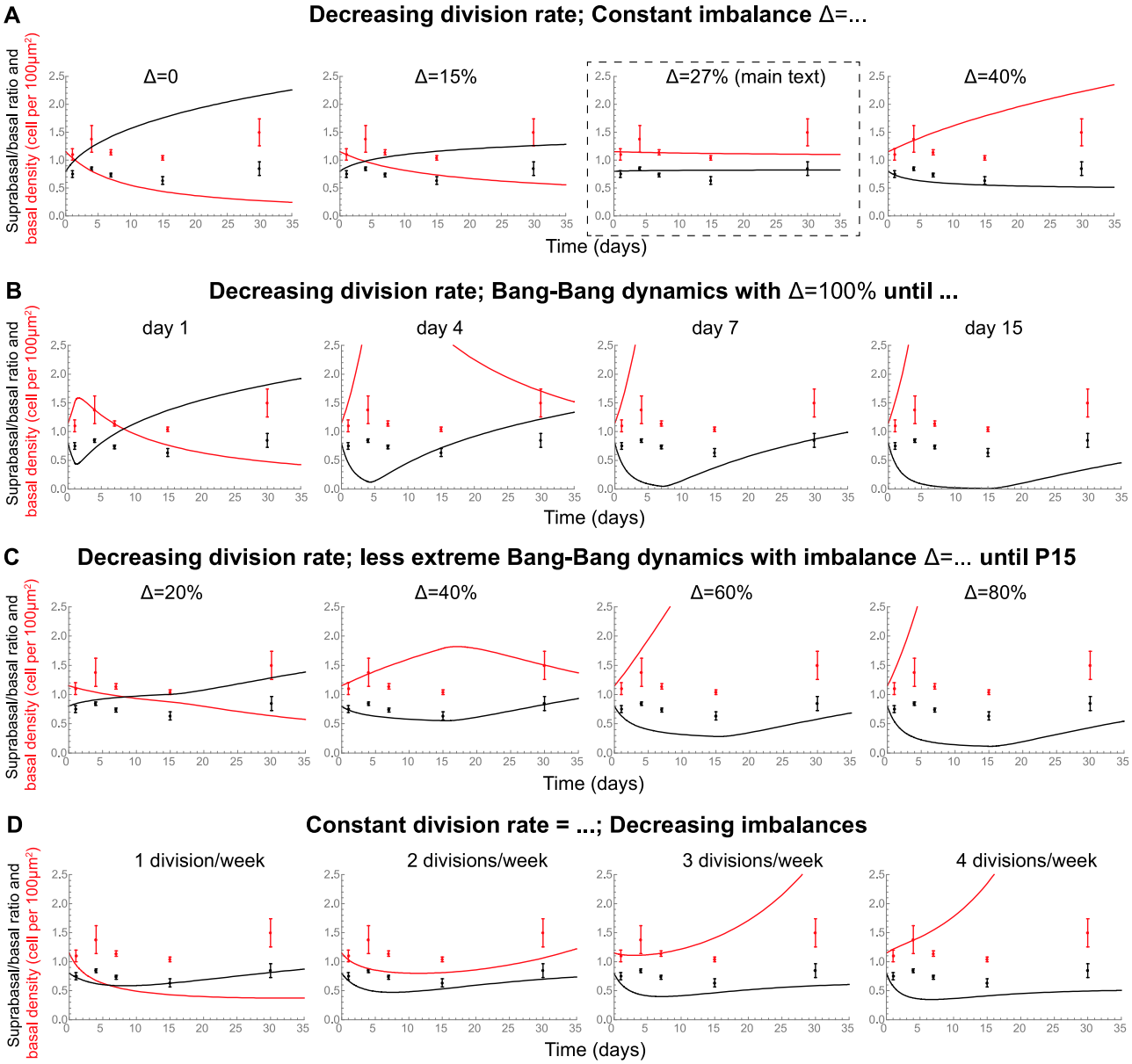

Figure S4. Simulation of BC Density and Basal to Suprabasal Ratio According to the Different Theoretical Models, Related to Figure 5

Comparison between model prediction and data (both shown for interscale). Black: suprabasal/basal ratio, red: basal density in cell per μm^2. (A) Influence of the value of constant imbalance $\Delta = 0,\ 15,\ 27,\ 40\%$ (with continually adjusting division rate as in main text), showing for instance that imbalances of 15% or 40% produce highly different predictions, while an imbalance of 27% produces harmonious growth with constant basal and suprabasal densities (B) Predictions of bang-bang dynamics (transition from $\Delta = 100\%$ to 0% imbalance at varying time points: P1, P4, P7 and P15) together with a continually decreasing division rate (as in main text), producing a vast excess of BCs. (C) Prediction of a "soft" bang-bang dynamics (transition from varying, partial imbalance values $\Delta = 20, 40, 60, 80\%$ to $\Delta = 0\%$ at P15), which again provides poor fits to the data, in particular as it predict a drop of basal density post P15, not observed in the data. (D) Predictions for a continually adjusting/decreasing imbalance, together with a constant division rate, not observed in the data (resp. 1,2,3 and 4 divisions per week). Symbols, experimental data; lines, model prediction. Error bars: mean ± SD.

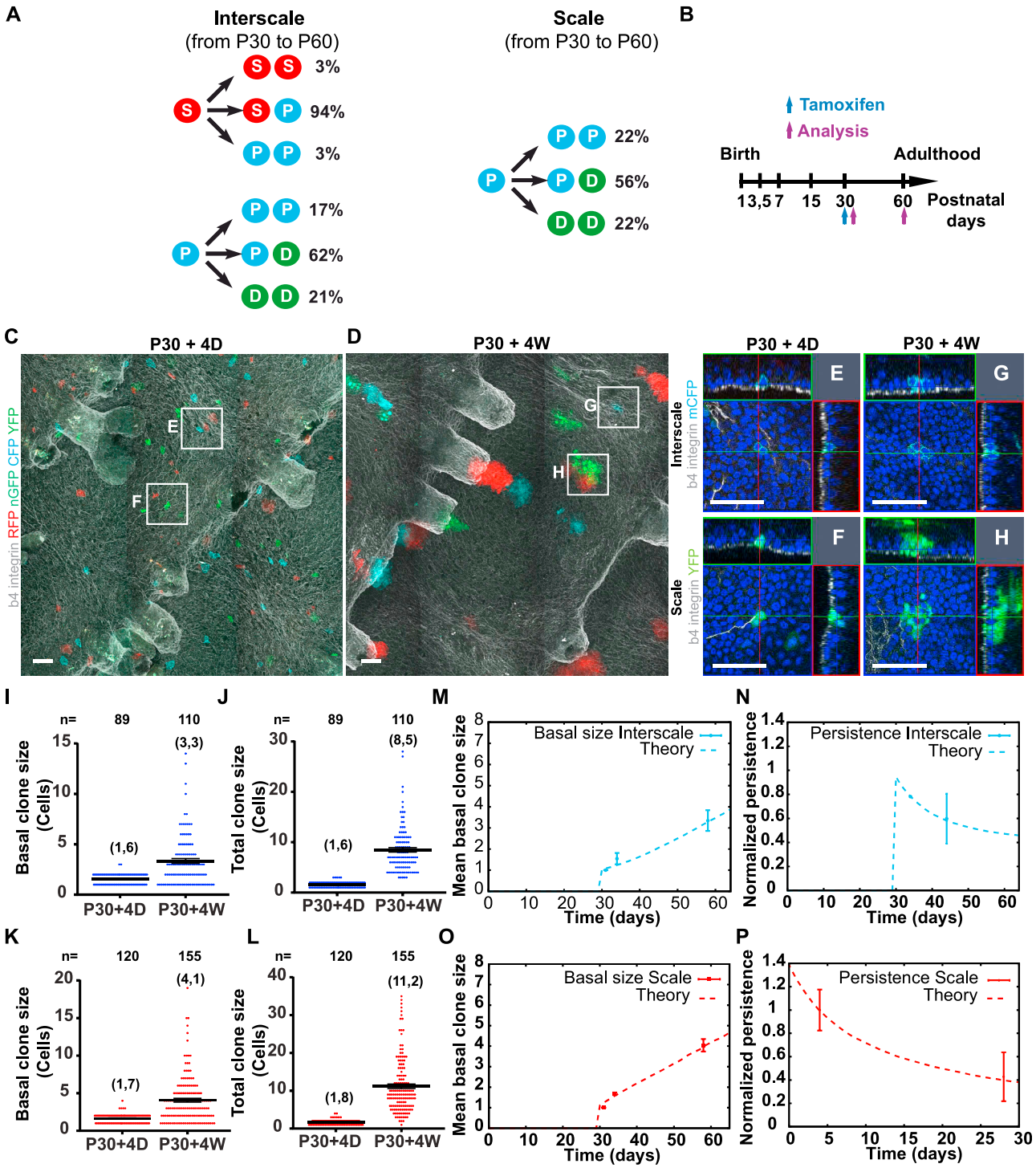

Figure S5. Transition between Postnatal Expansion and Adult Homeostasis, Related to Figure 4

(A) Model of the clonal dynamics governing scale and interscale homeostasis (Sánchez-Danés et al., 2016). (B) Experimental scheme of the clonal analysis performed at the time of the transition between the postnatal growth and adult homeostasis to challenge the theoretical model. (C-D) Representative *K14-CreER/Rosa-Confetti* whole-mount epidermis analyzed 4 days (C) and 4 weeks (D) after TAM injection at P30 (Maximum intensity projection of confocal images). (E-H) Confocal images of representative clones in interscale (E, G) and scale (F, H) 4 days and 4 weeks after TAM injection. Scale bar = 50μm. (I-L) Quantification of interscale (I, J) and scale (K, L) basal (I, K) and total (J, L) clone size over time at P30. N: number of clones analyzed from 5 mice, brackets: average clone size. (M-P) The model predicts well the basal clone size expansion (M, O) and the clonal persistence (N, P) in interscale and the scale at the different time points. Symbols, experimental data; dashed lines, model prediction. Data are represented as mean ± SEM.

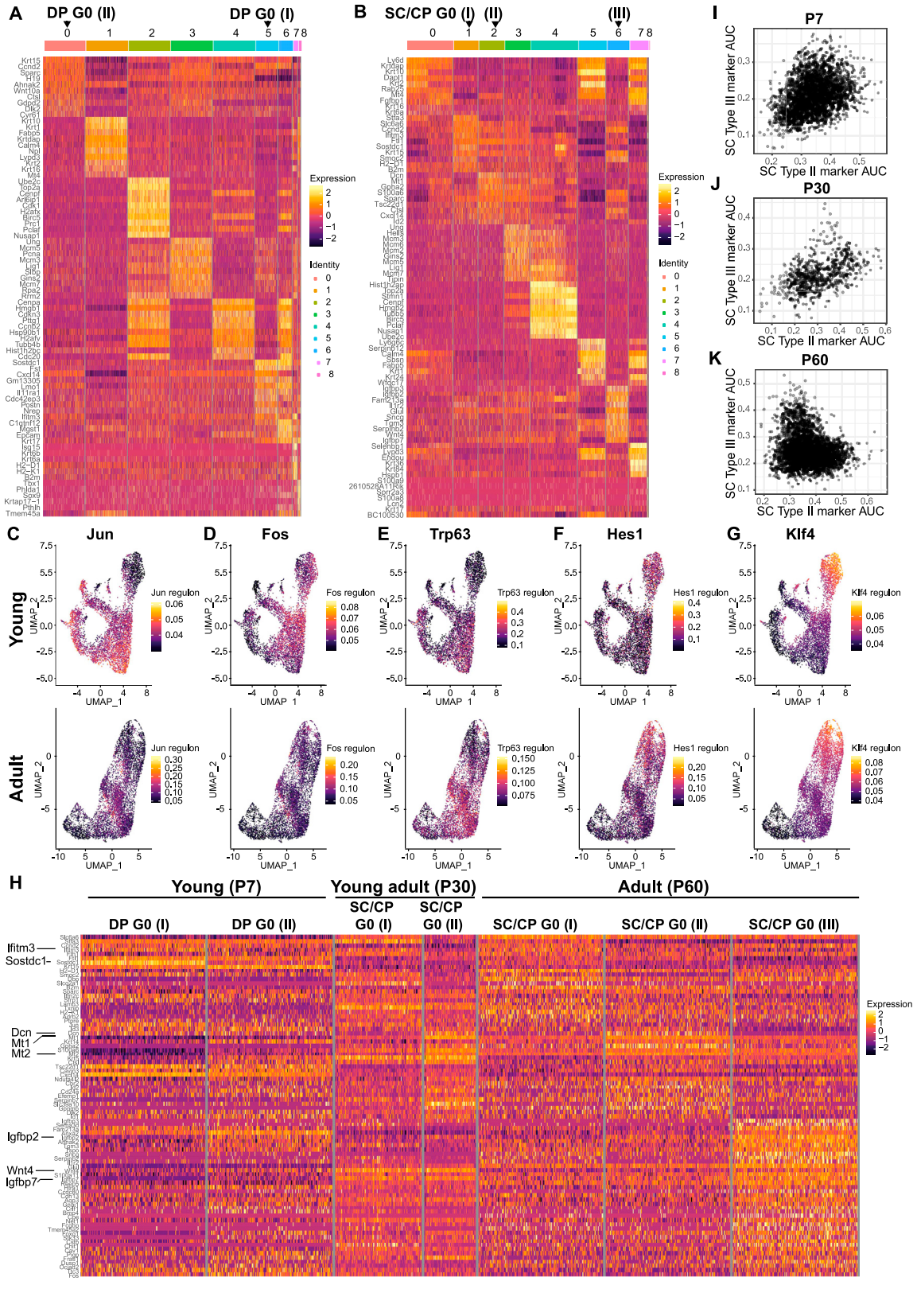

(legend on next page)

Figure S6. Single-Cell RNA Sequencing of DPs in Young Samples and Stem/Progenitors in Adult Samples, Related to Figure 6

(A-B) Heatmap showing the relative expression of the genes defining the different populations in young (A) and adult (B) samples. DP G0 and SC/CP G0 populations are shown with arrows. (C-G) UMAP dimensionality reduction plots colored by the degree of regulon activation for transcription factors differentially activated (AUC rank-sum test FDR corrected p value < 0.05) in DP G0 I (C) and DP G0 II (D) or both (E) and in differentiated cells (F,G) in young (upper panel) and adult (lower panel). Color scaling:AUC value of target genes in the regulon being expressed as computed by SCENIC. (H) Heatmap showing the relative expression of the genes identified in adult SC/CP populations in non-cycling BCs at P7, P30 and P60. Rows represent marker genes for P60 SC/CP subpopulations with a log-fold change in expression greater than 0.3. Columns represent cells belonging to DP clusters at P7 and SC/CP clusters at P30 and P60. The color of the cells represent normalized expression values for each gene-cell combination. P7 and P60 samples were subsampled to 200 cells each respectively. (I-K) Scatterplots of marker gene set enrichment. Dots represent individual cells in DP clusters at P7 (I) and SC/CP clusters at P30 (J) and P60 (K). The x axis represents the AUC values computed for each cell using the AUCell package and describe how high they express the P60 SC/CP G0 II marker genes whereas the y axis represents AUC values for the SC/CP G0 III marker genes. Linear correlations between the two AUC values is linked to sensitivity of detection and is correlated with the number of detected genes. Cells following a diagonal trend represent cells that homogeneously express the two sets of markers while cells deviating from the trend represent cells expressing distinct transcriptional marker gene signatures.

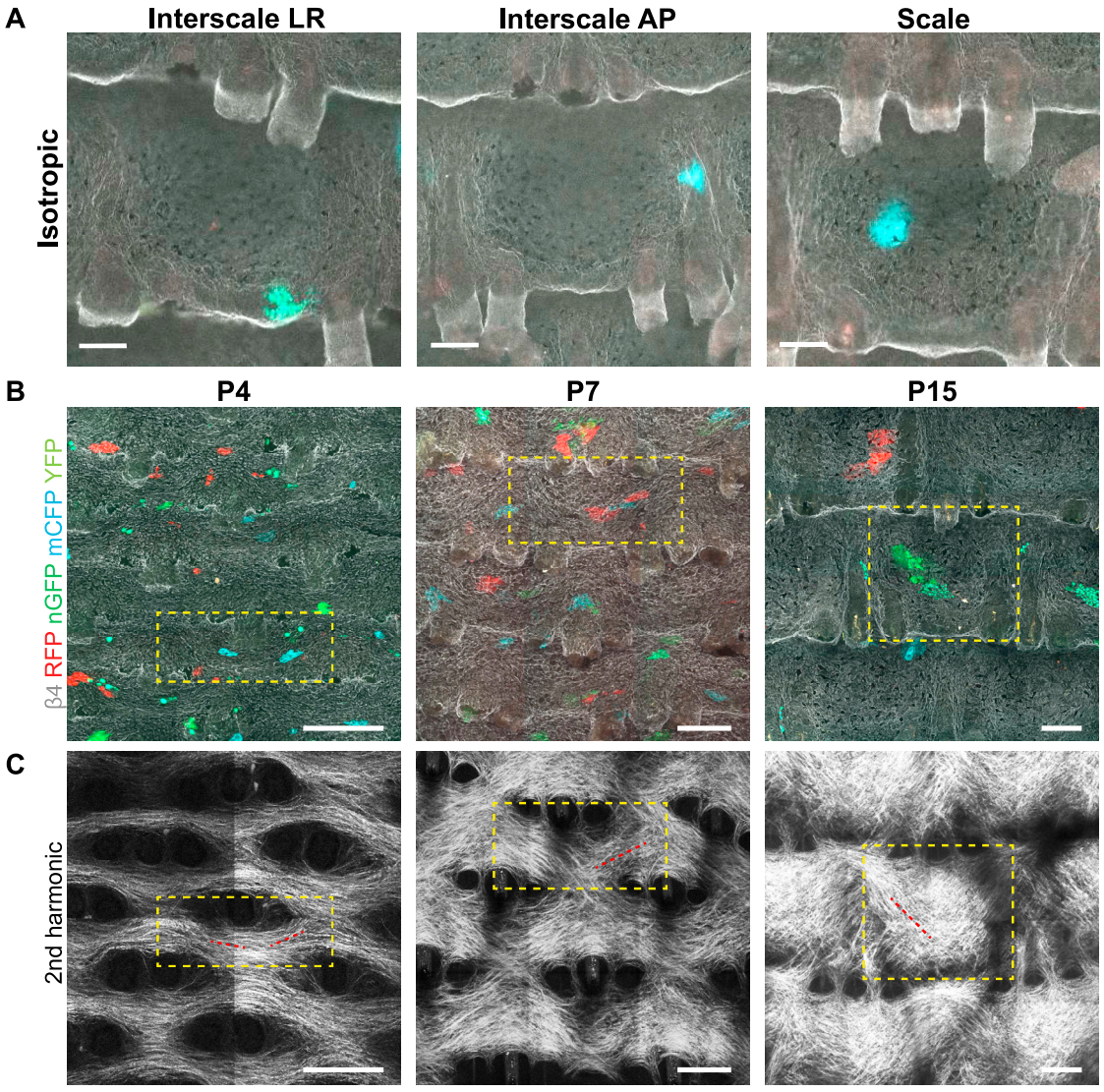

Figure S7. Clone Shape and Mechanical Constraints during Postnatal Skin Expansion, Related to Figure 7

(A) Whole-mount tail skin epidermis showing isotropic clones in the different regions of the tail IFE at P30 in a *K14-CreER*/*Rosa-Confetti* mouse induced at P1 (Maximum intensity projection of confocal pictures). (B-C) Whole-mount epidermis (B) and second harmonic signal highlighting fibrillary collagen in similar area (C) collected from mice aged of P4, P7 and P15. Yellow dotted square, hair follicle area with the scale in the center; red dotted lines, orientation of the collagen fibers. Note the preferential orientation of the clone along the collagen fibers. Scale bar = 100μm.